RSC Advances

PAPER

View Article Online
View Journal | View Issue

Cite this: *RSC Adv.*, 2026, **16**, 16564

Graphene-silver hybrid nanoparticle embedded phase change materials for enhanced thermal management of lithium-ion batteries

Balan Akshay, [a] Faisal Seyas Seyas Mumthas, [a] Manu Mohan, [a] Vishnu Bhuvanachandran Rajeswari *[a] and C. Ravikumar *[b]

Effective thermal regulation of lithium-ion battery (LIB) modules requires phase change materials (PCMs) with enhanced heat transfer capability without compromising latent heat storage. In this study, graphene nanoplatelet-silver (GNP-Ag) hybrid nanoparticles (NPs) were synthesized and incorporated at a low loading (0.1 wt%) into a paraffin-based PCM and evaluated using 3.0 mm and 6.0 mm cavity test rigs simulating battery module configurations. Compared to the base PCM, the hybrid composite exhibited a 20.37% enhancement in thermal conductivity (0.325 *vs.* 0.270 W m^{-1} K^{-1}). The complete melting time was reduced by 17.26% in the 3.0 mm cavity configuration, while the overall heat transfer rate increased by 12.60% and 15.50% in the 3.0 mm and 6.0 mm cavities, respectively, demonstrating improved performance under both conduction and convection dominated regimes. Further, the composite exhibited a maximum overall heat transfer coefficient of 448.8 W m^{-2} K^{-1} and a Nusselt number of 2.07, marking a transition from a conduction-dominated to a convection-enhanced regime during the phase transition. In particular, the energy storage capacity increased significantly, reaching 1775.93 J in the 6.0 mm cavity compared to 892.15 J for the base PCM. The composite maintained stable phase change behaviour with low Stefan numbers (0.026–0.047), demonstrating a favourable balance between latent and sensible heat storage. Importantly, a comprehensive uncertainty analysis, performed following ISO/IEC GUM and ASME PTC standards, confirmed that the observed enhancements were statistically significant and within acceptable experimental error limits, thereby validating the reliability of the reported thermal improvements. These enhancements were achieved at minimal NP loading, ensuring cost-effectiveness and scalability, and thereby establishing the developed GNP-Ag hybrid NP embedded PCM as a reliable and economically viable solution for advanced LIB thermal management systems.

Received 22nd December 2025
Accepted 5th March 2026

DOI: 10.1039/d5ra09895e

rsc.li/rsc-advances

1 Introduction

In the pursuit of revolutionizing energy storage and enhancing the performance of lithium-ion batteries (LIBs), effective thermal management within battery modules has become a critical priority. LIBs are extensively used in electric vehicles (EVs), portable electronics, and renewable energy systems owing to their high energy density and long cycle life;[1] however, ensuring thermal stability remains a significant challenge for maintaining safety and reliability.[2] Numerous studies have explored the fundamental science and recent advancements in LIBs, underscoring the need to address existing limitations and develop next-generation systems with enhanced safety, sustainability, and efficiency.[3] Research efforts have particularly focused on reducing costs, increasing energy and power density, and designing innovative electrode materials and architectures to mitigate challenges such as volume expansion and low conductivity.[4,5] Additionally, studies have highlighted the crucial role of LIBs in facilitating the transition from internal combustion engine vehicles to EVs and enabling large-scale energy storage for sustainable power systems.[6] To ensure peak performance, safety, and long-term stability, these batteries must operate within an optimal temperature range of approximately 20 °C to 50 °C.[7,8]

In this context, as the demand for higher energy density and faster charging rates continues to grow, effective thermal management of LIBs has become increasingly critical.[9] Excessive heat generation during battery operation poses a multifaceted threat, compromising not only the performance but also the safety and lifespan of energy storage systems. This challenge underscores the urgent need for effective temperature regulation within battery modules.[10] Among the various thermal management strategies, phase change materials (PCMs) have emerged as a promising

[a]*Energy Research Lab, Department of Mechanical Engineering, Marian Engineering College (MCE), Kazhakuttom, Thiruvananthapuram 695582, Kerala, India. E-mail: vishnu@marian.ac.in; Tel: +91-989 5575793*

[b]*Department of Chemical Engineering, Indian Institute of Technology Dharwad (IIT Dharwad), Dharwad 580 011, Karnataka, India. E-mail: ravikumar@iitdh.ac.in; ravikumarc2006@gmail.com; Tel: +91-836 2309741*

solution to address the thermal challenges due to their ability to absorb and release substantial amounts of latent heat during solid–liquid phase transitions, thereby providing passive thermal regulations.[11] However, to fully harness their potential, innovative strategies are required to enhance their energy storage density, minimize volumetric changes during phase transitions, and reduce thermal losses to the surroundings.[12,13]

To address these limitations, several studies have highlighted the potential of integrating nanoparticles (NPs) into PCMs to enhance their thermal performance, particularly through improvements in thermal conductivity. For instance, Hayat *et al.*[14] reported a significant enhancement in thermal conductivity by incorporating a hybrid of graphene nanoplatelets (GNPs) and multi-walled carbon nanotubes (MWCNTs) into a PCM, observing a nearly linear increase with increasing particle concentration. Trisnadewi *et al.*[15] demonstrated improved thermal conductivity and phase change stability by incorporating 0.5 wt% graphene and MAXene into soy wax. Radhakrishnan and Sobhan[16] investigated the effects of embedding GNPs and GNP-silver (Ag) hybrid NPs into PCMs, reporting a 52% increase in thermal conductivity; however, their study did not comprehensively address other key parameters relevant to battery thermal management, such as energy storage density or overall heat transfer behavior. Similarly, Yarmand *et al.*[17] studied GNP-Ag hybrid NPs and reported a 22.22% enhancement in thermal conductivity at 0.1 wt% concentration at 40 °C. Rufuss *et al.*[18] highlighted the superior thermal performance of NP-enhanced paraffin compared to base paraffin in solar still applications. More recently, the optimization of battery thermal management systems (BTMS) has evolved from fundamental material-level studies toward advanced multi-physics modeling and structural design strategies. A recent study emphasized the importance of coupling effects, particularly thermal-fluid-magnetic regulation mechanisms, in optimizing the performance of composite PCMs.[19] Concurrently, another study demonstrated that honeycomb-like microchannel heat sinks integrated with PCM to improve heat exchange area and temperature uniformity.[20] Furthermore, advanced numerical investigations have examined the effectiveness of internal and external PCM placement strategies for cylindrical battery configurations.[21] Despite these advancements, achieving comparable thermal performance enhancements using ultra-low loading passive hybrid fillers remains a significant challenge. Although existing studies convincingly demonstrate that NP additives can improve PCM thermal conductivity, many of them focus on generalized or application-specific contexts, such as solar thermal systems, rather than directly addressing the complex thermal management requirements of battery modules.[22,23] Therefore, comprehensive investigations are still required to evaluate not only thermal conductivity but also overall heat transfer performance, energy storage capacity, and reliability of NP-embedded PCMs under realistic battery operating conditions.

The majority of PCMs used in latent thermal energy storage systems suffer from inherently low thermal conductivity, which significantly limits their practical performance.[24] This limitation reduces the heat transfer rate between the heat transfer fluid and the PCM, thereby diminishing the overall energy storage and release efficiency of the system, prolonging the time required for complete melting and solidification.[25] The incorporation of NPs into PCMs has emerged as a promising strategy to address these shortcomings. Owing to their high surface-area-to-volume ratio and superior intrinsic thermal conductivity, NPs can substantially enhance heat transfer during both melting and solidification processes.[26] However, while such enhancements improve thermal diffusion through the formation of conductive networks, it is important to note that the simultaneous increase in dynamic viscosity of nanocomposite PCMs may suppress buoyancy-driven natural convection, potentially offsetting the gains achieved through improved conductivity. Therefore, the overall thermal response is governed by the interplay between enhanced conductive pathways and possible attenuation of liquid-phase convection. In the present study, an ultra-low loading (0.1 wt%) was strategically selected to ensure that the synergistic thermal pathways and micro-convection effects induced by the GNP-Ag hybrid NPs dominate over viscous suppression. This optimization enables improved heat transfer performance while preserving latent heat storage capacity, ultimately leading to enhanced energy storage density and overall system efficiency. Moreover, the ability to control and optimize these thermophysical properties by varying the type, size, and concentration of NPs provides a versatile approach for optimizing PCM performance for specific applications.[27,28] Thus, comprehensive investigations of NP-enhanced PCMs within battery modules are essential for designing efficient, reliable, and cost-effective thermal energy storage systems.

Accordingly, the present study aims to synthesize and characterize GNP-Ag hybrid NPs and incorporate them into a paraffin-based PCM for enhanced thermal management of LIB modules. The work systematically investigates the influence of ultra-low NP loading (0.1 wt%) and cavity dimensions (3.0 mm and 6.0 mm), representing realistic battery geometries,[29] on the thermophysical and heat transfer characteristics of composite PCM. Through detailed analyses of temperature distribution, liquid fraction evolution, energy storage capacity, and dimensionless heat transfer parameters including the Nusselt, Rayleigh, Stefan, and Fourier numbers; the study elucidates the synergistic role of GNP-Ag hybrid NPs in enhancing thermal conductivity, phase transition kinetics, and overall heat transfer. Furthermore, a detailed uncertainty analysis in accordance with ISO/IEC Guide 98-3:2008 (GUM) is performed to ensure the statistical reliability and reproducibility of all measured parameters. Overall, this study provides new insights into the rational design and application of hybrid NP-embedded PCMs for efficient and reliable thermal management in LIB modules, thereby contributing to the development of safer and high-performance energy storage systems.

2 Materials and methods

2.1 Materials

Stearic acid ($CH_3(CH_2)_{16}COOH$, 99% purity) and paraffin Wax (99% purity), with a melting point in the range of 58–60 °C, were

procured from Qualigens, India. Silver nitrate ($AgNO_3$) and sodium borohydride ($NaBH_4$, 98% purity) were purchased from Chemical House, India. Graphene nanoplatelet (GNP) aggregates, characterized by submicron particles with a surface area of 500 m^2 g^{-1}, were obtained from Alfa Aesar, India. Milli-Q water was used as the solvent for all the synthesis procedures.

2.2 Synthesis of GNP-Ag hybrid NPs and GNP-impregnated PCMs

The synthesis protocol for GNP-Ag hybrid NPs was followed according to Radhakrishnan and Sobhan.[16] In a typical experiment, 25 mg of GNP aggregates were dispersed in 50 mL of water and subjected to ultrasonication for 3 h, followed by magnetic stirring for an additional 3 h to ensure uniform dispersion. Subsequently, $AgNO_3$ crystals were added to the dispersion at a concentration of 1 mM, corresponding to a GNP : $AgNO_3$ ratio of 1 : 3 for the synthesis of GNP-Ag hybrid NPs. The *in situ* reduction of $AgNO_3$ as described in eqn (1), was initiated by the dropwise addition of 10 mL of 5 mM ice-cold $NaBH_4$ to the dispersion under continuous stirring.

$$2AgNO_3 + 2NaBH_4 + 6H_2O \rightarrow 2Ag^0 + 7H_2 + 2B(OH)_3 + 2NaNO_3 \quad (1)$$

After the complete addition of $NaBH_4$, stirring was stopped, and the dispersion was maintained in an ice bath for 15 minutes to ensure complete reduction. The resulting GNP-Ag hybrid NPs were collected by centrifugation, thoroughly washed with water, and dried overnight in an oven at 70 °C. The synthesis sequence is schematically illustrated in Fig. 1.

For the preparation of the base PCM, paraffin wax (97 wt%) and stearic acid (3 wt%) were melted together in a beaker at 65 °C. To prepare GNP-Ag hybrid NP embedded PCMs, GNP-Ag hybrid NPs were dispersed into the molten PCM at a loading of 0.1 wt% (Fig. 1). Dispersion homogeneity was achieved using a combination of magnetic stirring and ultrasonication. After the synthesis, the GNP-Ag hybrid NP embedded PCMs were stored in sealed containers to prevent exposure to ambient conditions.

2.3 Characterization

The structural phase analysis of the GNP-Ag hybrid NPs was carried out using an X-ray diffractometer (XRD) [Rigaku Minifex 600 equipped with an XPERT-3 diffractometer system) with Cu Kα_1 target (λ = 1.54 Å]. The scanning range was set from 2θ = 4.99° to 90.0° with a step size of 0.013°, and each step was held constant for 30.345 s. The morphology of the GNP-Ag hybrid NPs was examined using a field-emission scanning electron microscope (FESEM, Hitachi SU6600). The presence of Ag on the GNPs was confirmed through energy dispersive spectroscopy (EDS) using a Horiba EMAX system operating at 137 eV, integrated with the SEM. The thermophysical properties of the prepared base PCM, GNP embedded PCM and GNP-Ag hybrid NP embedded PCM were evaluated using different techniques. The specific heat capacities (solid and liquid phases) and latent heat of solidification were determined using a T-history method.[16] The melting onset and peak temperatures of the samples were measured using a differential scanning calorimeter (Setaram Setline DSC, KEP Technologies) at a heating rate of 5 °C min^{-1}. The instrument specifications include an

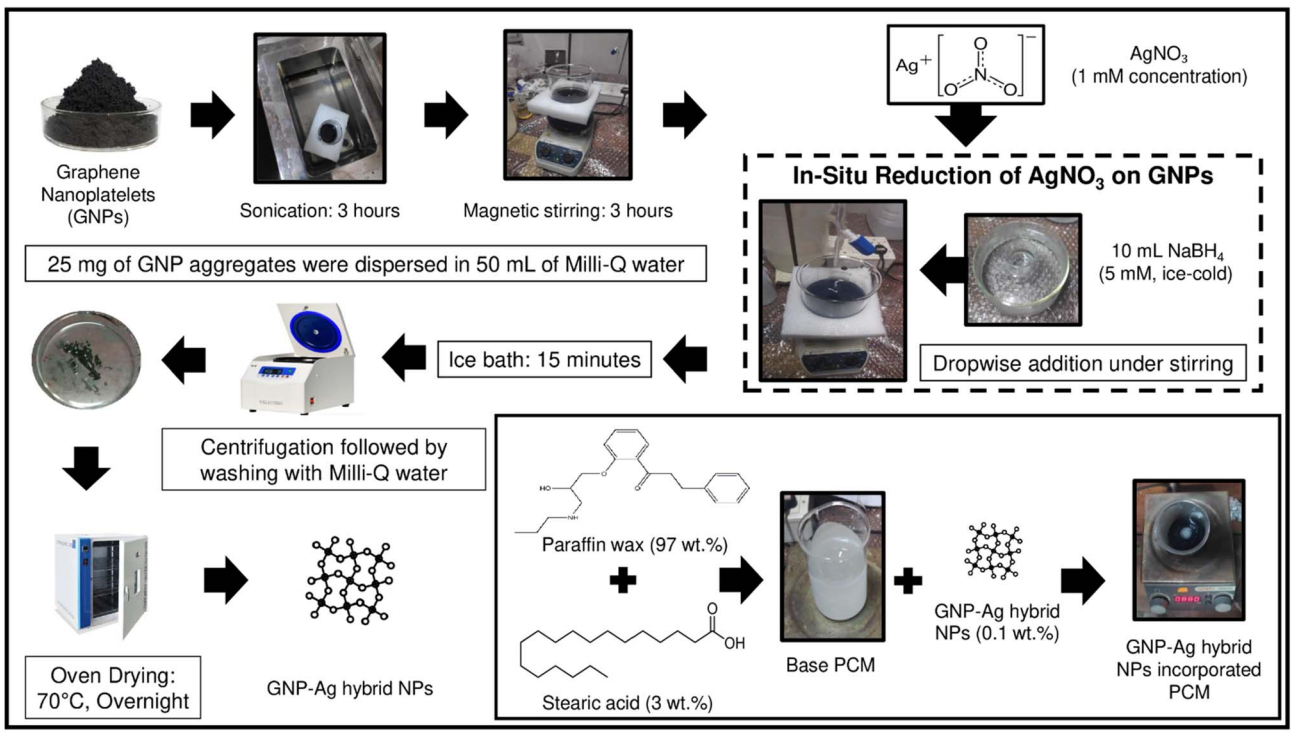

Fig. 1 Schematic illustrating the synthesis procedure of GNP-Ag hybrid NPs and GNP-Ag hybrid NPs embedded PCM.

enthalpy accuracy of ±0.8% (precision ±2.5%) and a temperature accuracy of ±0.30 °C (precision ±0.50 °C).

Thermal conductivity measurements were conducted using a transient planar source method (Hot Disk-TPS 500 S, Sweden) with a Kapton Sensor (5465 F2). As described in the SI file, measurements were conducted at an output power of 25 mW with a 5 s heat pulse at an initial temperature of 33 °C, ensuring an accuracy better than 5%. The dynamic viscosity measurements were carried out using a Rheometer (Brookfield LVDV-III Ultra Cone Plate Rheometer, USA) over a temperature range of 60 to 75 °C. Detailed experimental parameters including the use of a Cone Spindle CPE-40, a sample volume of 0.5 mL, and a constant shear rate of 7.5 s^{-1} are provided in the SI file, along with the instrument accuracy of ±1% of the full scale range (FSR). The weighted average densities of the samples were calculated using the effective density model proposed by Yu *et al.*,[30] utilizing manufacturer-provided density value for paraffin wax, stearic acid, Ag and GNPs.

2.4 Test rig setup and heat flux studies

The experimental setup, as depicted in Fig. 2a, was designed to emulate the specifications of 32 700 lithium iron phosphate ($LiFePO_4$, 3.2 V 6000 mAh, 3C) cells, consisting of a vertical concentric cylindrical configuration with a diameter of 32 mm and a height of 70 mm. The outer surface of the rig was insulated using aluminum silicate ceramic fiber (thermal resistance up to 2300 °F) to minimize heat dissipation, thereby closely simulating the thermal conditions within battery modules. The inner copper cylinder was used to replicate the thermal environment of the battery core. For temperature monitoring, T-type thermocouples (0.3 mm diameter) were strategically positioned at four radial points and connected to a data acquisition system (DAQ, Agilent 34972A LXI with 20 channel multiplexer, India), as shown in Fig. 2b. T-type thermocouples (blue, 30 SWG single-strand, double Teflon insulated; Thermotronic Instruments, India) were selected due to their excellent repeatability within the temperature range of −200 °C to 200 °C. The exposed (heated) junction length of each thermocouple was minimized to ensure high measurement accuracy.

The experimental configuration included the cavity thicknesses of 3.0 mm and 6.0 mm rigs to reflect realistic battery module geometries. The system was integrated with a high-density electrical heater housed within copper pipes, along with a wattmeter and a dimmerstat for controlled heat input (Fig. 2b). The precise positions of the four T-type thermocouples were defined by their radial coordinates to ensure spatial accuracy and consistency. As illustrated in the cross-sectional view (Fig. 2c), two thermocouples were placed at the interface of the inner copper wall ($r_1 = 16$ mm) to measure the heater wall temperature ($T_{w,i}$), while the remaining two were positioned at the outer boundary of the PCM cavity ($r_2 = 19$ mm for the 3.0 mm rig and $r_2 = 22$ mm for the 6.0 mm rig) to record the outer surface temperature ($T_{p,o}$).

This setup allowed for controlled heat generation within the system. Rigorous monitoring procedures were implemented to uphold the desired heat flux and ensure precise temperature measurements. Optimal thermal contact between the thermocouples and both the heater and PCM surfaces was maintained throughout the experiments to enhance measurement reliability. Continuous monitoring ensured stable heat flux conditions, providing a consistent foundation for experimental analysis. The wattmeter and dimmerstat facilitated accurate control of heat input, enabling the maintenance of predefined thermal parameters. Overall, the experimental design was structured to replicate realistic operating conditions while ensuring strict control, validity, and reproducibility in evaluating thermal management performance for battery applications.

3 Uncertainty analysis

The uncertainty evaluation framework incorporates detailed instrumentation specifications, measured thermophysical properties, temperature–time responses, DSC analysis, liquid fraction evolution, energy storage capacity calculations, and dimensionless number correlations. The analysis was performed in strict accordance with internationally recognized standards, namely ISO/IEC Guide 98-3:2008 (GUM)[31] and ASME PTC 19.1-2013,[32] to ensure statistical reliability and reproducibility of the results.

3.1 Mathematical framework for uncertainty propagation

The quantification of measurement uncertainty is based on the law of propagation of uncertainty, as prescribed by ISO/IEC Guide 98-3:2008 (GUM) and ASME PTC 19.1-2013 protocols. This framework ensures that the experimental data obtained for NP-enhanced PCMs are statistically robust and that the reported performance enhancements are clearly distinguishable from measurement uncertainty and experimental noise.

3.1.1 General functional relationship. The measurand Y (the theoretical quantity being determined) is generally not obtained through direct measurement but is instead determined from N input quantities $X_1, X_2, \ldots X_N$ through a functional relationship f. The measurement result, or the estimate of the measurand denoted by y, is therefore calculated by applying this function to the corresponding input estimates $x_1, x_2, \ldots x_N$ obtained during the experimental trials:

$$y = f(x_1, x_2, \ldots, x_N) \quad (2)$$

3.1.2 Combined standard uncertainty. The combined standard uncertainty, $u_c(y)$ represents the estimated standard deviation of the measurement result y. It is determined by combining the individual standard uncertainties of all input quantities using a first-order Taylor series expansion:

$$u_c^2(y) = \sum_{i=1}^{N} \left(\frac{\partial f}{\partial x_i}\right)^2 u^2(x_i) + 2\sum_{i=1}^{N-1}\sum_{j=i+1}^{N} \left(\frac{\partial f}{\partial x_i}\right)\left(\frac{\partial f}{\partial x_j}\right) u(x_i, x_j) \quad (3)$$

In this expression, $\frac{\partial f}{\partial x_i}$ are the sensitivity coefficients, which describe how the output estimate y varies with changes in the input estimates x_i. The term $u(x_i)$ represents the standard

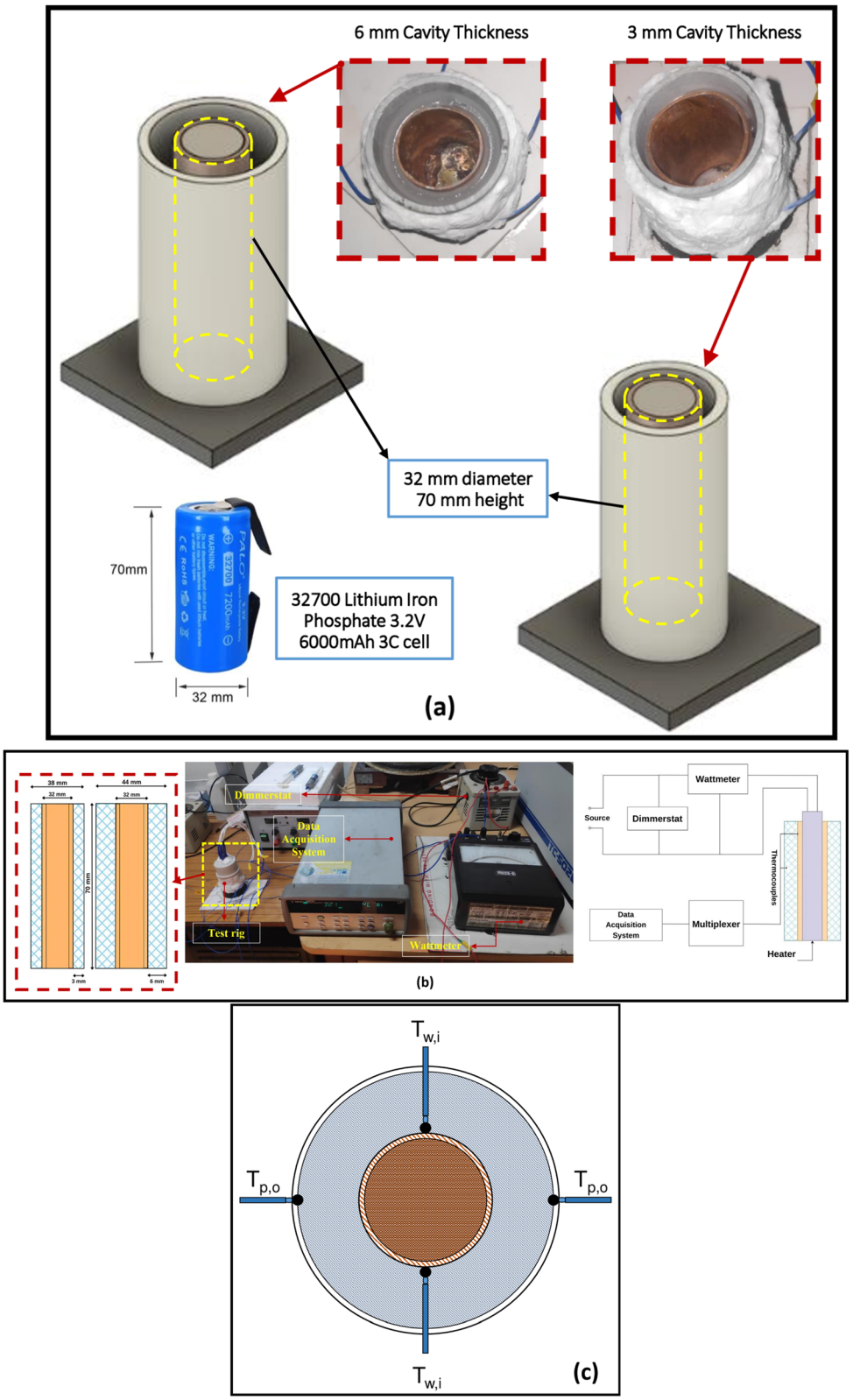

Fig. 2 (a) Test rigs with 3.0 mm and 6.0 mm cavity thickness, (b) experimental setup used for the temperature measurements with schematic representation and (c) cross-sectional schematic illustrating the 90-degree radial offset and boundary positioning of the four thermocouples at the inner wall of the heater $T_{w,i}$ and the outer PCM surface $T_{p,o}$.

uncertainty of each input, while $u(x_i,x_j)$ represents the covariance between pairs of input quantities, accounting for potential correlations.

3.1.3 Simplification for uncorrelated inputs. In the present study of PCM thermal analysis, the input quantities are assumed to be uncorrelated. This assumption is justified as the thermophysical properties were obtained from separate, independently calibrated instruments using distinct measurement principles and methodologies.

Accordingly, the covariance terms are considered negligible, and eqn (3) simplifies to the root-sum-of-squares (RSS) form:

$$u_c(y) = \sqrt{\sum_{i=1}^{N} \left(\frac{\partial f}{\partial x_i} u(x_i) \right)^2} \quad (4)$$

This simplified expression forms the mathematical foundation for all uncertainty evaluations presented in this work.

3.1.4 Expanded uncertainty and confidence intervals. To provide a statistically meaningful range for scientific comparison, the expanded uncertainty, denoted as $U(y)$, is employed. While the combined standard uncertainty $u_c(y)$ represents the standard deviation of the measurement result, the expanded uncertainty defines an interval that is expected to encompass the true value of the measurand with a high level of probability. It is calculated as:

$$U(y) = k_p^* \cdot u_c(y) \quad (5)$$

where, k_p^* is the coverage factor determined by the desired level of confidence p. For a normal (Gaussian) distribution, the standard choice in thermal sciences is $k_p^* = 2$, which corresponds to a confidence level of approximately 95%.

Under this framework, it can bestated with 95% probability that the true value of the measurand Y, lies within the interval defined by:

$$y - U(y) \leq Y \leq y + U(y) \quad (6)$$

This approach ensures that the reported differences between baseline PCMs and NP-enhanced formulations are statistically significant and represent actual physical changes in the material rather than artifacts of experimental uncertainty.

3.2 Instrumentation and measurement uncertainty specifications

The uncertainty analysis framework systematically integrates both Type A (random) and Type B (systematic) sources of measurement uncertainty to ensure high metrological fidelity. Type A uncertainties were quantified through repeated experimental trials followed by statistical analysis of the observed variability, whereas Type B uncertainties were derived from manufacturer specifications, calibration certificates, and traceable reference standards. All contributing components were propagated using the mathematical framework outlined in Section 3, in strict compliance with the Guide to the Expression of Uncertainty in Measurement (GUM, ISO/IEC 98-3:2008). This comprehensive approach ensures that both stochastic fluctuations and instrumental biases are rigorously represented in the combined standard uncertainty.

Expanded uncertainties were determined using a coverage factor of $k_p^* = 2$, corresponding to a 95% confidence level, for all directly and indirectly measured thermophysical parameters including temperature, thermal conductivity, specific heat, latent heat, viscosity, and dimensionless correlations. This methodology ensures statistical reliability, traceability, and transparent benchmarking of GNP-Ag hybrid NP enhanced PCMs against baseline formulations.

A Comprehensive Instrumentation Uncertainty Matrix (Table 1) consolidates the entire measurement infrastructure used for thermal characterization. Each entry specifies the instrument or methodology employed, detailed technical specifications, quantified uncertainty values (expanded, $k_p^* = 2$), and corresponding calibration or international reference standards. This structured approach establishes a transparent and traceable uncertainty budget across all experimental subsystems.

3.2.1 Temperature measurement uncertainty. The primary temperature sensing element employed in this study was a Type T (Copper-Constantan) thermocouple, conforming to IEC 60584-2:2013 Thermocouples, Part 2: Tolerances.[33,34] According to the Class 1 limits of error, the permissible deviation is $\pm$(0.5 °C or $0.004|T|$), whichever is greater, within the operational range of -40 °C $\leq T \leq$ +125 °C. At approximately room temperature ($\sim$25 °C), this corresponds to $\pm$0.5 °C, which was adopted as the baseline tolerance in the present uncertainty budget for temperature measurement. Temperature acquisition was performed using an Agilent 34972A Data Acquisition/Switch Unit. For Type T thermocouples, the manufacturer specifies a temperature measurement accuracy of $\pm$1.0 °C and a cold junction compensation (CJC) accuracy of $\pm$0.8 °C (typical).[35,36] Both values are reported as expanded uncertainties at the 95% confidence level. These specifications were incorporated as Type B uncertainty components in accordance with ISO/IEC Guide 98-3 (GUM, 2008), Section 4.3.3.

An additional uncertainty contribution arising from thermal contact resistance, probe placement variability, and immersion depth was considered. This component was modeled using a rectangular distribution with a half-width of $\pm$0.30 °C, consistent with the recommendations of NIST Technical Note 1297,[37] and Holman.[38] These references recommend treating placement-related effects as Type B contributions to account for spatial temperature gradients and contact mismatches between the thermocouple junction and the measured medium.

All individual contributors' thermocouple tolerance ($\pm$0.50 °C, 95% confidence level), DAQ accuracy ($\pm$1.0 °C, 95%), CJC accuracy ($\pm$0.8 °C, 95%), and placement effects ($\pm$0.30 °C, rectangular distribution) were statistically combined using the root-sum-square (RSS) method, as prescribed by the GUM framework. The resulting combined standard uncertainty was calculated as $u_c(T) = \pm 0.71$ °C, which, when expanded using a coverage factor of $k_p^* = 2$, yields an overall expanded temperature uncertainty, $U(T) = \pm 1.42$ °C (95% confidence level). Although this expanded uncertainty exceeds the individual IEC Class 1 tolerance limits, primarily due to DAQ accuracy, it

Table 1 Complete instrumentation uncertainty matrix

Parameter	Instrument/method	Detailed specification	Uncertainty, $U(y)$, $k_p^* = 2$	Standard
Temperature (T)	T-type thermocouples + Agilent 34972A DAQ	30 SWG, 0.3 mm dia, double Teflon insulated, 1.5 m long; 20-channel multiplexer	±1.42 °C	ISO/IEC Guide 98-3:2008 (GUM), ASME PTC 19.3 TW-2016, NIST TN 1297
Thermal conductivity (k)	TPS 500 S	Transient plane source method	±5%	NIST SRM 1450d
Specific heat of solids ($C_{p,s}$)	T-history method	Radhakrishnan & Sobhan methodology[16]	±4.8%	Reference standard
Specific heat of liquid ($C_{p,l}$)	T-history method	Radhakrishnan & Sobhan methodology[16]	±5.4%	Reference standard
Latent heat of solidification (H_s)	T-history method	Radhakrishnan & Sobhan methodology[16]	±5.3%	Reference standard
Mass (m)	Radwag AS 220.R2 balance	Analytical balance, 0–220 g range	±0.00023 g	OIML E2 weights
Radius/Length (r, L)	Mitutoyo 530-118, Vernier caliper	0–200 mm range, 0.02 mm resolution, ±0.03 mm accuracy	±0.0000346 m	Grade A, gauge blocks
Viscosity (μ)	Brookfield Rheometer	Rotational viscometry	±1% of the full-scale range (FSR)	NIST standards
DSC onset temperature (T_o)	Setaram-Setline DSC	Differential scanning calorimetry	±0.30 °C	Indium standard
DSC peak temperature (T_p)	Setaram-Setline DSC	Differential scanning calorimetry	±0.50 °C	Indium standard

ensures traceability, reliability, and methodological consistency in the temperature measurement process.

3.2.2 Dimensional and mass measurement uncertainty evaluation. Linear dimensions were measured using a Mitutoyo 530-118 Vernier caliper (manufacturer accuracy ±0.03 mm), with calibration verified using Grade A gauge blocks traceable to NIST standards. Following the ISO/IEC Guide 98-3:2008 (GUM) framework, the manufacturer's specification was treated as a rectangular probability distribution. The corresponding standard uncertainty was therefore estimated as $u_c(r,L) = a/\sqrt{3} = 0.0173$ mm, and the expanded uncertainty at a 95% confidence level was calculated as $U(r,L) = k_p^* \cdot u_c(r,L) = \pm 0.0346$ mm. This methodology adheres to the best international practices for Type B uncertainty evaluation as recommended by Taylor and Kuyatt.[37]

Mass measurements (m) were performed using a Radwag AS 220.R2 analytical balance, operating within a measurement range of 0–220 g. The manufacturer's linearity specification of ±0.0002 g was treated as a rectangular distribution, yielding a standard uncertainty of u_c(m) $0.002/\sqrt{3} = 0.000115$ g. The corresponding expanded uncertainty at the 95% confidence level was determined as $U(m) = k_p^* \cdot u_c(m) = 2 \times 0.000115 = 0.00023$ g. All type B uncertainties components were evaluated in accordance with ISO/IEC Guide 98-3:2008 (GUM), with calibration procedures traceable to OIML E2 class weights and national metrological standards.

4 Theoretical background

The density of the composite samples was determined using the classical rule of mixtures, in which the effective density is expressed as the weighted sum of the constituent densities. Accordingly, the composite density is given by:[30]

$$\rho = \sum_i w_i \rho_i \tag{7}$$

where w_i and ρ_i represent weight fractions and component densities, respectively. The corresponding sensitivity coefficients were obtained through partial differentiation, yielding $\frac{\partial \rho}{\partial \rho_i} = w_i$ and $\frac{\partial \rho}{\partial w_i} = \rho_i$. Based on these coefficients, the combined standard uncertainty in density, $u_c(\rho)$ is expressed as:

$$u_c(\rho) = \left[\sum_i [w_i \cdot u(\rho_i)]^2 + \sum_i [\rho_i \cdot u(w_i)]^2 \right]^{\frac{1}{2}} \tag{8}$$

The uncertainty analysis produced a combined standard uncertainty of $u_c(\rho) = 0.0099$ g cm^{-3}, corresponding to an expanded uncertainty of $U(\rho) = \pm 0.0198$ g cm^{-3} at a 95% confidence level (coverage factor of $k_p^* = 2$). This represents a relative uncertainty of ±2.2%, demonstrating strong agreement with theoretical mixture models typically applied to NP-enhanced PCM systems and confirming acceptable precision for composite characterization.

The investigation of heat transfer and phase change phenomena within PCMs and NP-impregnated PCMs is guided by a set of derived governing equations forming the theoretical foundation of this study. The equations are essential for analyzing and interpreting the observed thermal behaviors of the prepared materials. The steady-state heat conduction within a cylindrical sample quantifies the heat transfer rate Q through the material, where k is the thermal conductivity, $T_{w,i}$ and $T_{p,o}$

are the temperatures at the inner and outer radii r_1 and r_2, and l' is the length of the cylinder is given by.[39,40]

$$Q = 2\pi k l' \frac{(T_{w,i} - T_{p,o})}{\ln\left(\frac{r_2}{r_1}\right)} \quad (9)$$

The sensitivity coefficients were obtained *via* partial differentiation, where key terms include $\frac{\partial Q}{\partial k} = 2\pi l' \frac{(T_{w,i} - T_{p,o})}{\ln\left(\frac{r_2}{r_1}\right)}$, $\frac{\partial Q}{\partial T_{w,i}} = \frac{2\pi k l'}{\ln\left(\frac{r_2}{r_1}\right)}$ and additional terms for dimensional and temperature variables. The combined standard uncertainty for heat transfer rate, $u_c(Q)$ is expressed as:

$$u_c(Q) = \left[\left(\frac{\partial Q}{\partial k}\right)^2 u^2(k) + \left(\frac{\partial Q}{\partial l'}\right) u^2\left(l'\right) + \left(\frac{\partial Q}{\partial T_{w,i}}\right)^2 u^2(T_{w,i}) + \left(\frac{\partial Q}{\partial T_{p,o}}\right)^2 u^2(T_{p,o}) + \left(\frac{\partial Q}{\partial r_1}\right)^2 u^2(r_1) + \left(\frac{\partial Q}{\partial r_2}\right)^2 u^2(r_2)\right]^{\frac{1}{2}} \quad (10)$$

The expanded uncertainty associated with heat transfer rate determination was ±14.18% (95% confidence), consistent with experimental thermal transport studies involving cylindrical PCM configurations.

In the phase change analysis, the liquid fraction (f_l) (eqn (11)) characterizes the dynamic state of the material during melting. It represents the fraction of the material that exists in the liquid phase relative to the total volume. In the analysis of phase change phenomena, it is often assumed that the transition between solid and liquid phases occurs within a small temperature range, denoted as [T_s, T_l], as explained by Chen.[41] When the temperature (T) is below T_s, the material is in the solid phase. Conversely, if the temperature surpasses T_l, the material is in the liquid phase. In the intermediate temperature range ($T_s \le T \le T_l$), the material exhibits characteristics of a mixed phase or mushy zone. Accordingly, f is defined as follows:

$$f_l = \begin{cases} 0 & T < T_s \\ \frac{(T - T_s)}{(T_l - T_s)} & T_s \le T \le T_l \\ 1 & T > T_l \end{cases} \quad (11)$$

To evaluate the measurement uncertainty, sensitivity coefficients were derived through partial differentiation of f_l with respect to each temperature variable. The principal coefficients were identified as $\frac{\partial f_l}{\partial T} = \frac{1}{(T_l - T_s)}$, $\frac{\partial f_l}{\partial T_s} = \frac{(T - T_l)}{(T_l - T_s)^2}$, $\frac{\partial f_l}{\partial T_s} = \frac{(T_s - T)}{(T_l - T_s)^2}$. Using these coefficients, the combined standard uncertainty of liquid fraction, $u_c(f)$ is expressed as:

$$u_c(f_l) = \left[\left(\frac{1}{(T_l - T_s)}\right)^2 u^2(T) + \left(\frac{(T - T_l)}{(T_l - T_s)^2}\right) u^2(T_s) + \left(\frac{(T_s - T)}{(T_l - T_s)^2}\right) u^2(T_l)\right]^{\frac{1}{2}} \quad (12)$$

The expanded uncertainty in liquid fraction determination reached ±34.8% (95% confidence), reflecting the intrinsic difficulty of accurately characterizing phase distribution within the mushy zone. This high relative uncertainty represents a metrological limit for technical-grade organic waxes with narrow melting ranges; in such cases, the steep thermal gradient in the mushy zone mathematically amplifies the standard temperature uncertainty through the sensitivity coefficient, $\frac{\partial f_l}{\partial T}$. This finding is consistent with Saeed *et al.*,[42] who demonstrated that non-equilibrium thermal gradients in PCMs lead to significantly higher statistical variability than those observed in pure or standard materials.

Recognizing the significance of efficient thermal management, the present study focuses on a comprehensive evaluation of energy storage capacities over time, with a specific emphasis on identifying materials that not only possess a substantial capacity for storing thermal energy but also exhibit rapid responsiveness to changing thermal conditions. One critical aspect of thermal energy storage is the utilization of PCMs, which undergo a phase transition as they absorb or release thermal energy. The latent heat associated with this phase change is a key factor contributing to the effectiveness of thermal storage systems. In this context, latent heat is defined as the energy required for a material to undergo a phase change. Pagkalos *et al.*[43] provide a fundamental expression for the energy storage capacity ($Q_{\text{energy storage}}$) of a solid–liquid PCM in the form of latent heat storage, given by

$$Q_{\text{energy storage}} = m \cdot C_{p(s)} \cdot \Delta T_s + m \cdot H_f \cdot f_l + m \cdot C_{p(l)} \cdot \Delta T_l \quad (13)$$

where, the terms $C_{p(s)}$ and $C_{p(l)}$ represent the specific heat capacities in the solid and liquid states respectively, f_l is the fraction of sample melted, H_f is the latent heat of fusion ($H_f = |H_s|$), m is the sample masses utilized (m = 1.683 g for the 3.0 mm rig and m = 6.732 g for the 6.0 mm rig), and ΔT_s and ΔT_l are the temperature changes during the solid and liquid phases, respectively. The first term represents the sensible heat of the solid phase, the second term is the latent heat of fusion, and the third term accounts for the sensible heat of the liquid phase. The inclusion of latent heat in the formulation underscores the advantage of utilizing phase-change materials in thermal storage applications. This theoretical framework serves as a robust foundation for understanding the thermal behavior of materials in the context of energy storage.

Sensitivity coefficients were obtained through systematic partial differentiation of the governing expression for the energy storage capacity ($Q_{\text{energy storage}}$) with respect to each input parameter. The principal terms derived include

$\frac{\partial Q_{\text{energy storage}}}{\partial m} = C_{\text{p(s)}} \cdot \Delta T_{\text{s}} + H_{\text{f}} \cdot f_{\text{l}} + C_{\text{p(l)}} \cdot \Delta T_{\text{l}}$, representing the sensitivity of energy storage to variations in sample mass, and $\frac{\partial Q_{\text{energy storage}}}{\partial H_{\text{f}}} = m \cdot f_{\text{l}}$, which quantifies the contribution of latent heat during the phase transition. Additional sensitivity coefficients were determined for all other independent variables to ensure complete uncertainty propagation across the sensible and latent heat regions. Accordingly, the combined standard uncertainty associated with the total energy storage capacity, $u_{\text{c}}(Q_{\text{energy storage}})$ is expressed as:

$$u_{\text{c}}\left(Q_{\text{energy storage}}\right) = \left[\left(\frac{\partial Q_{\text{energy storage}}}{\partial m}\right)^2 u^2(m) + \left(\frac{\partial Q_{\text{energy storage}}}{\partial C_{\text{p(s)}}}\right)^2 u^2\left(C_{\text{p(s)}}\right) + \left(\frac{\partial Q_{\text{energy storage}}}{\partial \Delta T_{\text{s}}}\right)^2 u^2(\Delta T_{\text{s}}) + \left(\frac{\partial Q_{\text{energy storage}}}{\partial f_{\text{l}}}\right)^2 u^2(f_{\text{l}}) + \left(\frac{\partial Q_{\text{energy storage}}}{\partial H_{\text{f}}}\right)^2 u^2\left(H_{\text{f}}\right) + \left(\frac{\partial Q_{\text{energy storage}}}{\partial C_{\text{p(l)}}}\right)^2 u^2\left(C_{\text{p(l)}}\right) + \left(\frac{\partial Q_{\text{energy storage}}}{\partial \Delta T_{\text{l}}}\right)^2 u^2(\Delta T_{\text{l}})\right]^{\frac{1}{2}} \quad (14)$$

The energy stored during solid-phase heating exhibits an expanded uncertainty of ±13.55% (95% confidence level), primarily governed by solid-phase specific heat measurement precision and temperature quantification accuracy. The energy stored during phase transition demonstrates a substantially higher expanded uncertainty of ±70.4%, attributed to the intrinsic complexity of liquid fraction determination (±34.8%) within the mushy zone, where minor temperature variations yield pronounced phase redistribution due to steep thermal gradients characteristic of the narrow melting range (5 °C). This liquid fraction uncertainty, contributing 99.7% to the latent heat uncertainty variance, arises from temperature measurement uncertainty (±0.71 °C, standard) amplified through the sensitivity coefficient $\frac{\partial f_{\text{l}}}{\partial T} = 0.2$ per °C. The liquid-phase sensible heat component carries expanded uncertainty of ±201%, though this has negligible influence on total uncertainty when liquid-phase heating is minimal (<0.1% of total energy) within the experimental time scale. The propagated total energy storage uncertainty is determined to be ±41.83% (95% confidence level), clearly dominated by phase transition quantification challenges inherent to mushy zone characterization.

The overall heat transfer coefficient (U_{overall}) and the Nusselt number (Nu) are critical parameters in characterizing heat transfer processes in natural convection as mentioned by Elsherbiny *et al.*[44] The heat transfer performance of the system is characterized by the overall heat transfer coefficient U_{overall}, which quantifies the cumulative effectiveness of the thermal pathway from the heat source into the storage matrix. This formulation traceably accounts for the total thermal resistance network, including conduction through the copper heating surface and the dynamic conductive-convective transport mechanisms within the PCM matrix. The overall heat transfer coefficient is defined as:

$$U_{\text{overall}} = \frac{Q^*}{A \cdot \Delta T} \quad (15)$$

where Q^* is the controlled heat generation rate, A is the surface area of the heater-PCM interface, ΔT is the temperature difference between the temperature at the inner wall of the heater ($T_{\text{w,i}}$) and the outer PCM surface ($T_{\text{p,o}}$).

The sensitivity coefficients of the overall heat transfer coefficient with respect to each independent parameter are expressed as $\frac{\partial U_{\text{overall}}}{\partial Q'} = \frac{1}{A \cdot \Delta T}$, $\frac{\partial U_{\text{overall}}}{\partial A} = -\frac{Q'}{A^2 \cdot \Delta T}$, $\frac{\partial U_{\text{overall}}}{\partial \Delta T} = -\frac{Q'}{A \cdot \Delta T^2}$. Accordingly, the combined standard uncertainty associated with the overall heat transfer coefficient, $u_{\text{c}}(U_{\text{overall}})$, is expressed as:

$$u_{\text{c}}(U_{\text{overall}}) = \left[\left(\frac{1}{A \cdot \Delta T}\right)^2 u^2\left(Q'\right) + \left(\frac{Q'}{A^2 \cdot \Delta T}\right)^2 u^2(A) + \left(\frac{Q'}{A \cdot \Delta T^2}\right)^2 u^2(\Delta T)\right]^{\frac{1}{2}} \quad (16)$$

The overall heat transfer coefficient determination yields an expanded uncertainty of ±20.07% (95% confidence level), calculated through propagation of uncertainties in heat flux measurement, surface area determination, and temperature difference quantification. The uncertainty magnitude is appropriate for natural convection measurements in PCM systems, where complex flow patterns and transient thermal boundary conditions introduce additional variability.

The Nusselt number (Nu) relates the characteristic length of the cavity (L), and thermal conductivity of sample (k) with U_{overall}. It is a dimensionless quantity that characterizes the enhancement of heat transfer due to convection compared to pure conduction, and is defined as:

$$\text{Nu} = \frac{U_{\text{overall}} L}{k} \quad (17)$$

Sensitivity coefficients were derived as $\frac{\partial \text{Nu}}{\partial U_{\text{overall}}} = \frac{L}{k}$, $\frac{\partial \text{Nu}}{\partial L} = \frac{U_{\text{overall}}}{k}$ and $\frac{\partial \text{Nu}}{\partial k} = -\frac{U_{\text{overall}} L}{k^2}$, yielding the combined standard uncertainty for Nusselt number, u_{c}(Nu):

$$u_{\text{c}}(\text{Nu}) = \left[\left(\frac{L}{k}\right)^2 u^2(U_{\text{overall}}) + \left(\frac{U_{\text{overall}}}{k}\right)^2 u^2(L) + \left(\frac{U_{\text{overall}} L}{k^2}\right)^2 u^2(k)\right]^{\frac{1}{2}} \quad (18)$$

The Nusselt number calculation exhibits an expanded uncertainty of ±22.42% (95% confidence level), propagated from uncertainties in heat transfer coefficient determination

(±20.07%), characteristic length measurement, and thermal conductivity evaluation. This uncertainty encompasses the fundamental challenges in dimensionless heat transfer analysis, where multiple uncertain parameters combine multiplicatively.

Understanding their relationships with the Rayleigh number (Ra) provides insights into the transition from laminar to turbulent flow and aids in predicting the heat transfer behavior of the samples in various applications,[44] and is defined as

$$\mathrm{Ra} = \mathrm{Gr}\cdot\mathrm{Pr} \tag{19}$$

where, Pr represents the Prandtl number and is defined as $\mathrm{Pr} = C_{\mathrm{p(l)}}\mu/k$ and Gr represents the Grashof number and is defined as $\mathrm{Gr} = \dfrac{g\beta(T_{\mathrm{w,i}} - T_{\mathrm{p,o}})\rho^2 L^3}{\mu^2}$. The g denotes acceleration due to gravity, β is the coefficient of thermal expansion, $T_{\mathrm{w,i}}$ and $T_{\mathrm{p,o}}$ are the heater and sample temperatures, ρ is density, μ is the viscosity and $C_{\mathrm{p(l)}}$ is specific heat. The combined standard uncertainty associated with the Rayleigh number, $u_{\mathrm{c}}(\mathrm{Ra})$ is expressed as:

$$u_{\mathrm{c}}(\mathrm{Ra}) = \left[(\mathrm{Pr})^2u^2(\mathrm{Gr}) + (\mathrm{Gr})^2u^2(\mathrm{Pr}) + 2(\mathrm{Pr})(\mathrm{Gr})u(\mathrm{Gr},\mathrm{Pr})\right]^{\frac{1}{2}} \tag{20}$$

The Rayleigh number determination carries an expanded uncertainty of ±23.02% (95% confidence level), reflecting the complex propagation of uncertainties from thermophysical properties and geometric parameters required for natural convection characterization.

For natural convection scenarios, the relationship between Nu and Ra is often expressed empirically as power-law correlations or obtained through experimental investigations. The Nusselt number (Nu), Stefan number (Ste), and Fourier number (Fo) are interconnected factors influencing heat transfer characteristics. The Fourier Number (Fo), where α is the thermal diffusivity of the sample and t denotes the characteristic time, a parameter representing the typical time scale associated with the melting process of the samples is defined as

$$\mathrm{Fo} = \alpha t/L^2 \tag{21}$$

Sensitivity coefficients were determined by partially differentiating the above equation with respect to each independent variable. The resulting coefficients are $\dfrac{\partial \mathrm{Fo}}{\partial \alpha} = \dfrac{t}{L^2}$, $\dfrac{\partial \mathrm{Fo}}{\partial t} = \dfrac{\alpha}{L^2}$, $\dfrac{\partial \mathrm{Fo}}{\partial L} = -\dfrac{2\alpha t}{L^3}$. Based on these coefficients, the combined standard uncertainty of the Fourier number, $u_{\mathrm{c}}(\mathrm{Fo})$ is given as:

$$u_{\mathrm{c}}(\mathrm{Fo}) = \left[\left(\frac{t}{L^2}\right)^2u^2(\alpha) + \left(\frac{\alpha}{L^2}\right)^2u^2(t) + \left(\frac{2\alpha t}{L^3}\right)^2u^2(L)\right]^{\frac{1}{2}} \tag{22}$$

The Fourier number exhibits an expanded uncertainty of ±14.85% (95% confidence level), dominated by thermal diffusivity uncertainty propagated from thermal conductivity, density, and specific heat measurements.

Stefan number (Ste), where $C_{\mathrm{p(l)}}$ is the specific heat of liquid phase in the melting process of the samples, ΔT is the difference between the temperature of inner and outer radii r_1 and r_2 during melting is defined as

$$\mathrm{Ste} = C_{\mathrm{p(l)}}\cdot\Delta T/H_{\mathrm{f}} \tag{23}$$

Sensitivity coefficients obtained through partial differentiation of the above relation are $\dfrac{\partial \mathrm{Ste}}{\partial C_{\mathrm{p(l)}}} = \dfrac{\Delta T}{H_{\mathrm{f}}}$, $\dfrac{\partial \mathrm{Ste}}{\partial \Delta T} = \dfrac{C_{\mathrm{p(l)}}}{H_{\mathrm{f}}}$, $\dfrac{\partial \mathrm{Ste}}{\partial H_{\mathrm{f}}} = -\dfrac{C_{\mathrm{p(l)}}\cdot\Delta T}{{H_{\mathrm{f}}}^2}$. Accordingly, the combined standard uncertainty associated with the Stefan number, $u_{\mathrm{c}}(\mathrm{Ste})$ is expressed as:

$$u_{\mathrm{c}}(\mathrm{Ste}) = \left[\left(\frac{\Delta T}{H_{\mathrm{f}}}\right)^2u^2\left(C_{\mathrm{p(l)}}\right) + \left(\frac{C_{\mathrm{p(l)}}}{H_{\mathrm{f}}}\right)^2u^2(\Delta T) + \left(\frac{C_{\mathrm{p(l)}}\cdot\Delta T}{{H_{\mathrm{f}}}^2}\right)^2u^2\left(H_{\mathrm{f}}\right)\right]^{\frac{1}{2}} \tag{24}$$

The determination of the Stefan number resulted in an expanded uncertainty of ±17.85% (95% confidence level), obtained through the propagation of uncertainties associated with all experimentally measured variables.

The Nusselt number captures the overall heat transfer intensity, while the product of Stefan and Fourier numbers (Fo.Ste) characterizes the efficiency of the transient energy storage process, identifying the rate at which latent heat is absorbed relative to the system's thermal diffusion limit.[45] This exploration aims to reveal how the interplay of overall heat transfer and transient heat conduction impacts the cumulative thermal characteristics of the system. The combined standard uncertainty associated with the product of Stefan and Fourier numbers, $u_{\mathrm{c}}(\mathrm{Fo.Ste})$ is expressed as:

$$u_{\mathrm{c}}(\mathrm{Fo.Ste}) = \left[(\mathrm{Ste})^2u^2(\mathrm{Fo}) + (\mathrm{Fo})^2u^2(\mathrm{Ste}) + 2(\mathrm{Fo})(\mathrm{Ste})u(\mathrm{Fo.Ste})\right]^{\frac{1}{2}} \tag{25}$$

The combined Fourier–Stefan number product exhibits an expanded uncertainty of ±23.22% (95% confidence level), representing the propagated uncertainties from both transient time scale (±14.85%) and phase change intensity (±17.85%) characterizations.

5 Results and discussions

5.1 Material characterization and synthesis validation

The synthesis of GNP-Ag hybrid NPs was comprehensively validated using XR, FESEM, and EDAX. The XRD pattern (Fig. 3a) of the synthesized GNP-Ag hybrid NPs exhibited peaks at 38.17°, 44.31°, 64.41°, 77.59°, and 81.52°, corresponding to the (111), (200), (220), and (311) crystallographic planes of face-

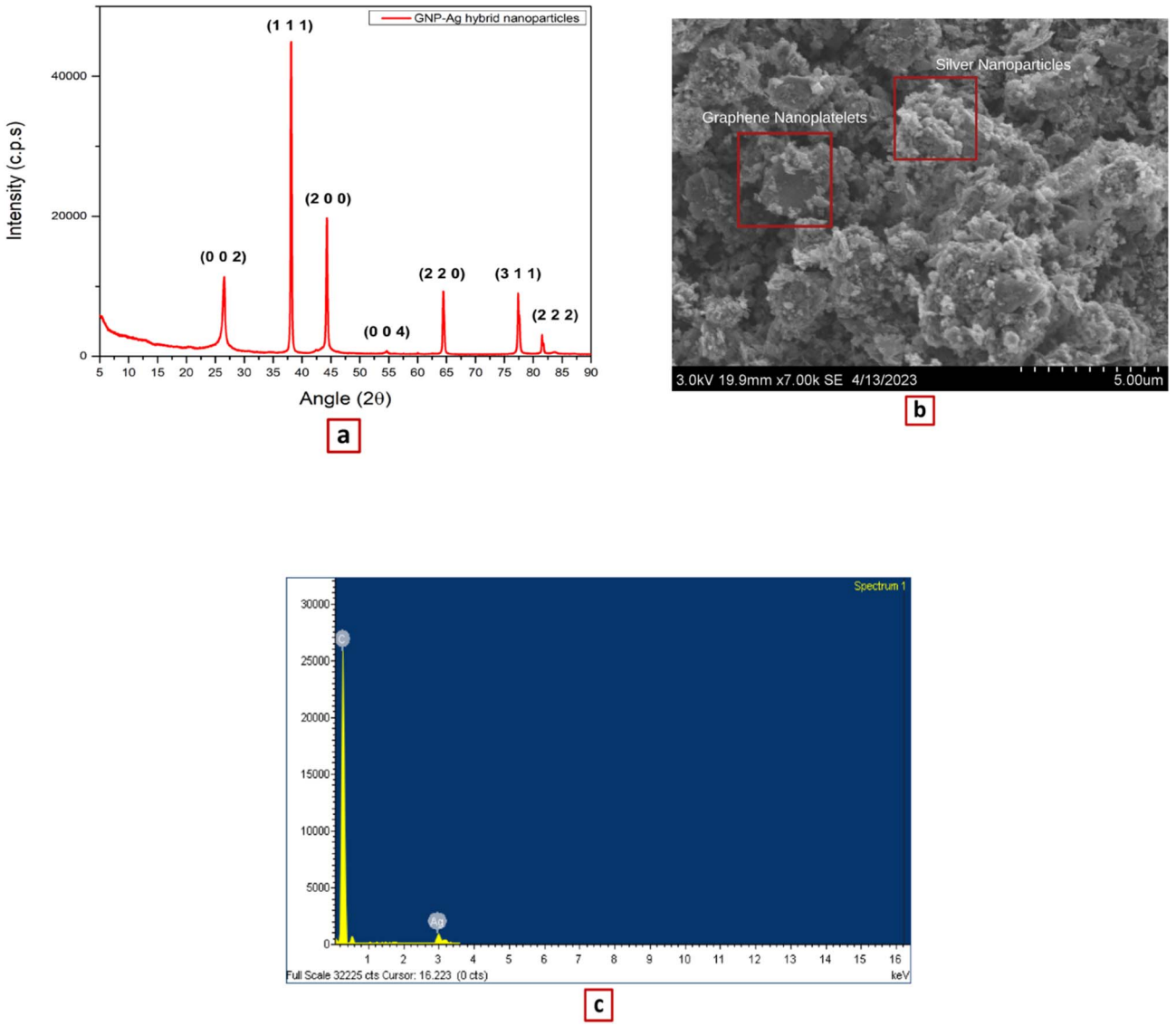

Fig. 3 (a) XRD pattern (b) FESEM image and (c) EDAX pattern of graphene nanoplatelets impregnated with silver particles (GNP-Ag hybrid NPs).

centered cubic Ag. In addition, prominent peaks observed at 26.52° and 54.22° corresponds to the crystalline planes (002) and (004) of graphite, respectively. The simultaneous detection of characteristic Ag and graphitic peaks confirms the successful formation of GNP-Ag hybrid NPs, indicating that Ag NPs were effectively embedded on to the GNP framework.

Morphological analysis through FESEM (Fig. 3b) further supports this conclusion. The micrographs clearly show bright, uniformly distributed Ag NPs deposited on the layered GNP surfaces. The Ag NPs appear well-dispersed, suggesting effective nucleation and growth during synthesis, which is critical for ensuring homogeneous thermal pathways in the composite. Complementing these findings, EDAX analysis (Fig. 3c) confirmed the presence of Ag in the composite.

The spectrum displays a dominant carbon (C) peak corresponding to the GNP substrate, along with a distinct Ag peak confirming the incorporation of metallic Ag. Quantitative EDAX analysis yielded weight percentages of 92.42% C and 7.58% Ag. The relatively low Ag signal intensity aligns with the intentionally low Ag loading (0.1 wt% relative to the PCM system), demonstrating controlled synthesis and preventing excessive agglomeration. These characterization results confirm the successful fabrication of GNP-Ag hybrid NPs with well-defined crystalline phases, uniform morphology, and verified elemental composition. The incorporation of FCC-structured Ag NPs onto thermally conductive GNP sheets establishes a hybrid architecture capable of enhancing phonon and electron transport pathways. Importantly, the minimal Ag loading (0.1 wt%) ensures economic feasibility and scalability while maintaining the desired thermal enhancement performance. This validated material synthesis provides a strong structural and compositional foundation for subsequent evaluation of the hybrid NPs in PCM-based thermal management applications.

Table 2 Thermophysical properties of base PCM and NP impregnated (0.1 wt%) PCMs

Samples	Specific heat ($J\ g^{-1}\ K^{-1}$)		Average density, ρ ($g\ cm^{-3}$)	Dynamic viscosity μ_d (mPa s)	Latent heat of solidification, H_s ($J\ g^{-1}$)	Thermal conductivity, k ($W\ m^{-1}\ K^{-1}$)
	$C_{p(s)}$	$C_{p(l)}$				
Base PCM	5.01	2.16	0.8982	4.95	147	0.270
Base PCM-GNPs	5.14	2.64	0.9004	6.91	140	0.301
Base PCM-GNP-Ag NPs	5.56	2.43	0.9006	6.52	144	0.325

5.2 Thermophysical properties evaluation

The thermophysical properties of the prepared base PCM, GNP embedded PCM (base PCM-GNPs), and GNP-Ag hybrid NP embedded PCM (base PCM-GNP-Ag NPs) were systematically evaluated using different techniques (refer to the SI file for the techniques) and are given in Table 2. These properties are essential for characterizing thermal storage behaviour and serve as fundamental input parameters for the theoretical and dimensionless analyses presented earlier. The key parameters assessed include specific heat capacity, average density, dynamic viscosity, latent heat of solidification, and thermal conductivity.

Dynamic viscosity measurements were conducted over the temperature range of 60–70 °C, corresponding to the fully molten state of the paraffin-based PCM (melting interval 58–60 °C). This post-melting regime is particularly relevant to lithium-ion battery thermal management, where elevated operating temperatures demand efficient heat dissipation. As illustrated in Fig. S1, all samples exhibited a consistent temperature-dependent decrease in dynamic viscosity, characteristic of thermally activated molecular mobility in molten organic materials. The reduction in viscosity with increasing temperature enhances internal fluid motion, thereby promoting improved convective heat transport. At 70 °C, the base PCM-GNPs displayed a comparatively higher dynamic viscosity than the base PCM-GNP-Ag NP system. This behavior can be attributed to the planar morphology and potential aggregation tendency of GNPs within the molten matrix, which may increase flow resistance and alter rheological behavior. In contrast, the Ag decoration in the GNP-Ag hybrid structure appears to improve NP dispersion and reduce interparticle interactions, thereby moderating viscosity while maintaining enhanced thermal conductivity pathways.

Thermal conductivity values showed marked improvements with NP inclusion, particularly for the GNP-Ag hybrid NP embedded PCM, which exhibited a 20.37% increase in thermal conductivity (0.325 $W\ m^{-1}\ K^{-1}$ *vs.* 0.270 $W\ m^{-1}\ K^{-1}$), directly enhancing the conductive component of the heat dissipation process. While density variations remained minimal and consistent with the addition of metallic Ag, the 0.1 wt% loading also increased the specific heat capacity, likely due to enhanced molecular interactions at the NP-PCM interface. Conversely, the latent heat of solidification decreased from 147 $J\ g^{-1}$ to a range of 140–144 $J\ g^{-1}$, which supports accelerated phase-transition kinetics and enhanced thermal responsiveness to transient heat loads in energy-storage applications. The improved rheological balance in the hybrid composite suggests a synergistic effect between GNPs and Ag NPs. While GNPs provide high in-plane thermal conductivity, the incorporation of Ag enhances interfacial contact and dispersion stability, leading to improved thermal responsiveness without excessively increasing viscous resistance. This optimized thermophysical profile is particularly advantageous for transient thermal management applications, where rapid heat absorption and redistribution are required under dynamic loading conditions.

5.3 Thermal performance analysis and dimensionless parameters

The heat transfer characteristics of the prepared base PCM, GNP embedded PCM (base PCM-GNPs), and GNP-Ag hybrid NP embedded PCM (base PCM-GNP-Ag NPs) were investigated under a constant heat flux of 624.45 $W\ m^{-2}$, using cylindrical cavities of 3.0 mm and 6.0 mm thickness. The thermal response was analyzed through temperature–time profiles, from which temperature distribution, stored heat rate, and melting behavior were evaluated. Temperature distribution describes the spatial and temporal variation of temperature within the PCM matrix. It provides insight into heat propagation dynamics, thermal gradients, and the uniformity of energy diffusion throughout the material. The stored heat rate represents the material's capability to absorb and release thermal energy during sensible and latent heat stages, thereby reflecting the effectiveness of thermal energy storage. Melting profiles characterize the phase transition process, including the onset of melting, melting duration, and transient fluctuations within the mushy zone. The comparative analysis focused on understanding the influence of NP impregnation on the thermal equilibrium behavior between the PCM matrix and the heater surface.

The incorporation of GNPs and GNP-Ag hybrid NPs in PCMs modifies the internal heat transfer pathways by enhancing effective thermal conductivity and promoting improved energy redistribution within the molten region.

The heater temperatures depicted in Fig. 4a and b were extracted from the temperature distribution plots. The nearly overlapping heater temperature curves for all samples indicate stable and uniform heating conditions across the experiments. The minimal deviation among profiles confirms that variations in melting behaviour and energy storage performance arise from material modifications rather than external thermal

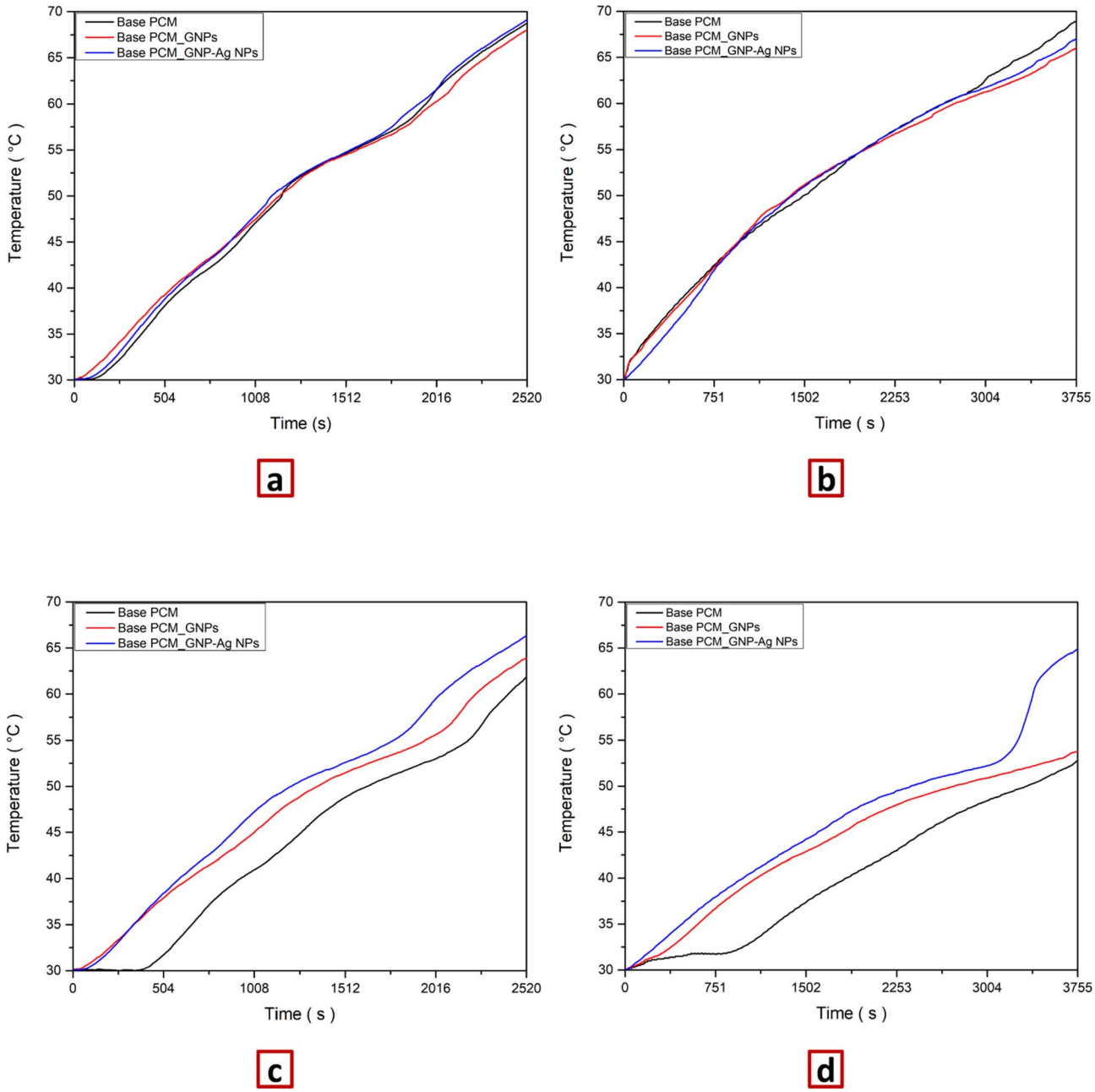

Fig. 4 Temperature–time graphs for (a) heater surface in 3.0 mm cavity test rig, (b) heater surface in 6.0 mm cavity test rig, (c) outer surface in 3.0 mm cavity test rig, and (d) outer surface in 6.0 mm cavity test rig.

inconsistencies. In the initial stages of heat absorption within the 3.0 mm cavity, the outer temperature–time profile of the base PCM exhibits an extended quasi-isothermal region lasting up to approximately 300 s (Fig. 4c). This behavior is primarily attributed to the material's high latent heat capacity, coupled with its relatively low thermal conductivity, which limits the initial rate of heat propagation through the solid matrix. In contrast, NP-embedded PCMs demonstrate a different thermal response; their enhanced conductivity and high surface area-to-volume ratios allow for significant latent heat absorption without a substantial initial temperature rise. A similar trend is observed in the 6.0 mm cavity (Fig. 4d), where the base PCM temperature remains consistent until 751 s before shifting as the material reaches phase change temperatures. This suggests that PCM initially absorbs heat primarily through sensible storage before transitioning to latent heat-dominated behavior.

The horizontal temperature plateau observed at approximately 30 °C in the base PCM heating profiles (Fig. 4c and d) is attributed to the endothermic solid–solid phase transition, commonly referred to as the 'rotator phase'. Technical-grade paraffin waxes undergo this polymorphic transition as the crystalline structure shifts from a rigid orthorhombic lattice to a hexagonal phase, allowing the hydrocarbon chains to rotate about their long axes.[46] This phenomenon provides a critical

initial thermal buffering stage, absorbing energy without a significant temperature rise before the onset of the primary solid–liquid phase change at ~56 °C. The attenuation of this plateau in the base PCM-GNP-Ag NP composites suggests that the NPs facilitate a more continuous thermal pathway, acting as heterogeneous nucleation sites that reduce the energy barrier for lattice rotation and promote a more rapid transition into the liquid state.[47] Consequently, the thermophysical properties reported in Table 2 account for this transition, as the specific heats and enthalpies determined *via* the T-history method capture the cumulative energy absorption of both the solid–solid and solid–liquid regimes. The transient temperature anomalies and minor fluctuations observed during the peak melting stage are attributed to the non-linear evolution of natural convection cells and the localized disruption of flow paths by the thermocouple probes. Such phenomena are characteristic of phase transitions within vertical cylindrical enclosures. As noted by Guarda *et al.*,[48] the physical presence of measurement probes can introduce localized thermal resistance or promote the adhesion of solid PCM to the probe surface. This disrupts the development of natural convection patterns, inducing transient fluctuations that are inherent to the experimental setup rather than indicative of instrumentation malfunction.

DSC analysis (Fig. 5) reveals a significant difference between the onset and peak melting temperatures of the NP-impregnated PCMs compared to the base PCM. These temperatures are crucial for efficient thermal management in energy storage applications. The base PCM exhibits the highest onset temperature (T_0 = 50.42 °C), indicating a higher energy barrier for initial melting. Interestingly, incorporating GNPs and GNP-Ag hybrid NPs resulted in a systematic decrease in the onset temperature by ~0.6 °C and ~0.7 °C, respectively (from Fig. 5). This suggests that the addition of NPs to the PCM could potentially facilitate the melting process by lowering the activation energy required.

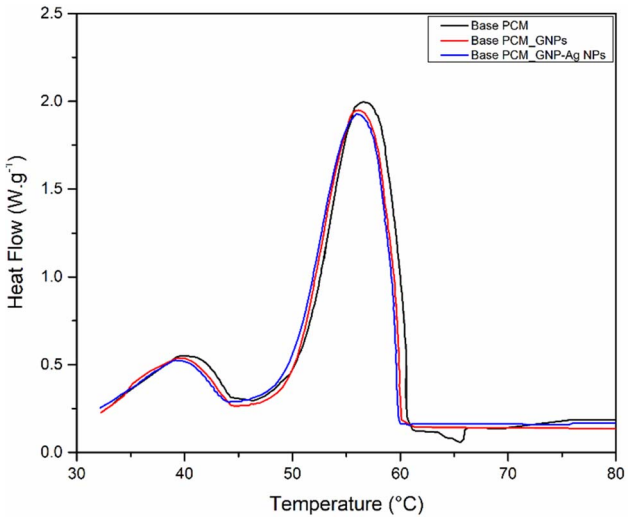

Fig. 5 Differential scanning calorimetry analysis of the prepared base PCM, GNP impregnated and GNP-Ag hybrid NP-impregnated PCM samples.

Further, the peak melting temperatures followed a similar trend, with the base PCM displaying the highest peak (T_p = 56.53 °C), followed by the GNP embedded PCM (56.15 °C) and GNP-Ag hybrid NP embedded PCM (55.93 °C) composites. While the decrease in peak temperatures is less pronounced compared to the onset temperatures, it could be attributed to a broadening of the melting peak in the composites, suggesting a less-defined melting process compared to the base PCM.[49] This phenomenon can be explained by considering both thermal conductivity and the temperature-dependent function NPs as nucleation sites.[50] Incorporating NPs generally enhances thermal conductivity, with GNP-Ag hybrid NPs showing greater enhancement compared to GNPs alone. Additionally, NPs serve as nucleation sites, reducing the energy barrier for PCM to melt. However, these sites become more active as temperature increases, exerting a more significant impact during the later stages of melting.[51] With rising temperatures, NPs become more effective in promoting the formation of liquid phase nuclei, thus facilitating a quicker and more complete transition to the liquid state at a lower peak temperature. Thus, the improved melting behavior positions of these NP-enhanced PCMs offer highly promising candidates for optimized thermal energy storage applications.

The introduction of 0.1 wt% GNP-Ag hybrid NPs into PCM notably increased heat transfer rates by 12.60% and 15.5% for the 3.0 mm and 6.0 mm cavities respectively, surpassing the effects of 0.1 wt% GNP alone which demonstrated a 3.47% and 6.67% rise calculated using eqn (9) (where $T_{w,i}$ and $T_{p,o}$ are derived from heater and outer surface temperature profiles as shown in Fig. 4). In comparison to NP-impregnated PCMs, the base PCM exhibited slower temperature gains, indicating the potential benefits of heightened thermal conductivity in improving overall heat transfer rates. This observation aligns with findings outlined in Table 2. The inclusion of GNP-Ag hybrid NPs led to the most significant enhancement in heat transfer, as evidenced by the improved melting rate and lower phase change temperature compared to other compositions. These findings emphasize the importance of NP impregnation in optimizing the thermal performance of PCMs, highlighting the potential for enhancing heat transfer efficiency in various applications.

Analyzing the liquid fraction is a critical parameter in battery thermal management, which quantifies the proportion of a PCM that has transitioned from a solid to a liquid state. A rapid increase in liquid fraction signifies efficient heat absorption, essential to mitigate temperature spikes within batteries. The liquid fraction data [calculated using eqn (11) and shown in Table 3] revealed a marked improvement in phase change kinetics for the NP-impregnated PCMs compared to the base PCM. Initially, all PCM compositions exhibited low liquid fractions, indicating a dominant solid phase. As the constant heat flux progressed, there is a gradual increase in the liquid fraction for each composition, reflecting the solid-to-liquid transition.

The GNP-Ag hybrid NP embedded PCM demonstrates the most rapid increase in the liquid fraction, reaching a complete liquid phase at 2085 s. In contrast, the GNP embedded PCM and

Table 3 Liquid fraction comparison during melting of base PCM, PCM impregnated with 0.1% GNPs, and PCM impregnated with 0.1% GNP-Ag hybrid NPs as a function of time in 3.0 mm cavity and 6.0 mm cavity test rigs

	Time, t (s)					
	3.0 mm cavity test rig			6.0 mm cavity test rig		
Liquid fraction, f_l	Base PCM	Base PCM-GNPs	Base PCM-GNP-Ag NPs	Base PCM	Base PCM-GNPs	Base PCM-GNP-Ag NPs
0	1675	1345	1185	3410	2695	2310
0.1	1825	1455	1290	3590	3040	2555
0.2	1970	1600	1435	3750	3375	2905
0.3	2100	1755	1570	3755>	3670	3135
0.4	2195	1905	1695		3755>	3220
0.5	2250	2015	1800			3270
0.6	2290	2100	1870			3300
0.7	2340	2150	1925			3325
0.8	2395	2195	1970			3355
0.9	2455	2250	2020			3380
1	2520	2320	2085			3400

the base PCM took a longer time to achieve the same state, with liquid fractions reaching completion at 2320 s and 2520 s, respectively. This trend signifies that incorporation of GNP-Ag hybrid NPs enhanced the PCM's ability to transition into a liquid state more rapidly, thus improving its overall thermal performance in terms of heat absorption and phase change efficiency. The liquid fraction comparison during melting in the 6.0 mm cavity showed similar trends observed as in the 3.0 mm cavity. However, due to the larger cavity size, the transition to a complete liquid phase further took longer time for all samples compared to the 3.0 mm cavity. In this case too, the GNP-Ag hybrid NP embedded PCM exhibited the fastest transition to a complete liquid phase, achieving this state at 3400 s. In contrast, GNP embedded PCM and base PCM showed mixed-phase liquid fractions at the same time, indicating a slower overall transition to the liquid state. The larger 6.0 mm cavity resulted in a slower transition to a complete liquid phase for all samples compared to the 3.0 mm cavity. This highlights the impact of volume on phase change behavior, as larger cavities require more time for complete PCM liquefaction. However, even in the larger cavity, GNP-Ag hybrid NP embedded PCM exhibited remarkable advantages, demonstrating the fastest transition and superior thermal management capabilities. The inclusion of GNP-Ag hybrid NPs enhances the thermal conductivity of PCM. This improved thermal conductivity facilitates more efficient heat distribution within the material during melting, leading to a faster and more complete transition from solid to liquid. Additionally, GNPs might act as nucleation sites, lowering the energy barrier for the phase change and promoting faster melting.

In the comprehensive investigation of the thermal behavior of various PCM compositions during complete melting, the present work further delved into the intricate details of their energy storage capacities, exploring the impact of NP inclusion on PCM performance designed for thermal management in battery modules, which function as thermal batteries, absorbing heat during battery operation (charging) and releasing it during discharge cycles to maintain optimal temperature conditions. Assessing energy storage capacity [measured in terms of Joules (J)] over time provides a more comprehensive perspective on the dynamic thermal performance of PCMs, capturing both latent and sensible heat contributions. This approach is particularly relevant for applications like passive cooling in battery modules, where optimizing thermal management is crucial.

The energy storage capacity of all the prepared PCMs [calculated using eqn (13)] reveals a significant improvement in energy storage and absorption rate for the NP impregnated PCMs, particularly the PCM impregnated with GNP-Ag hybrid NPs. The value demonstrated here is the point at which the samples experienced a higher storage capacity at the onset of complete melting ($f_l = 1$). In a smaller cavity configuration (3.0 mm) as shown in Fig. 6a, the base PCM achieved a storage capacity of 420.074 J at 2520 s (from Table 3 for $f_l = 1$). On the other hand, the base PCM loaded with 0.1 wt% GNPs exhibited a slightly improved performance, reaching 407.879 J within a faster time-frame of 2320 s at $f_l = 1$. Sensible heat during the liquid phase extends this capacity to 419.283 J. This indicates a faster absorption rate and potentially a more complete phase change due to the presence of GNPs. However, the PCM with GNP-Ag hybrid NPs demonstrated the most impressive performance, storing a remarkable 428.013 J within an even faster time frame of 2085 s at $f_l = 1$ and extended up to 451.040 J due to influence of sensible heat during liquid phase. This faster absorption and higher storage capacity highlights the potential benefits of both NP inclusion and the specific role of Ag in the GNP-Ag hybrid NPs. The improvement in energy storage was due to the inclusion of NPs, which became even more pronounced in a larger cavity test rig (6.0 mm) as shown in Fig. 6b. In this setting, the PCM embedded with GNP-Ag hybrid NPs not only experienced complete melting but also exhibited an exceptional energy storage capacity, reaching an impressive

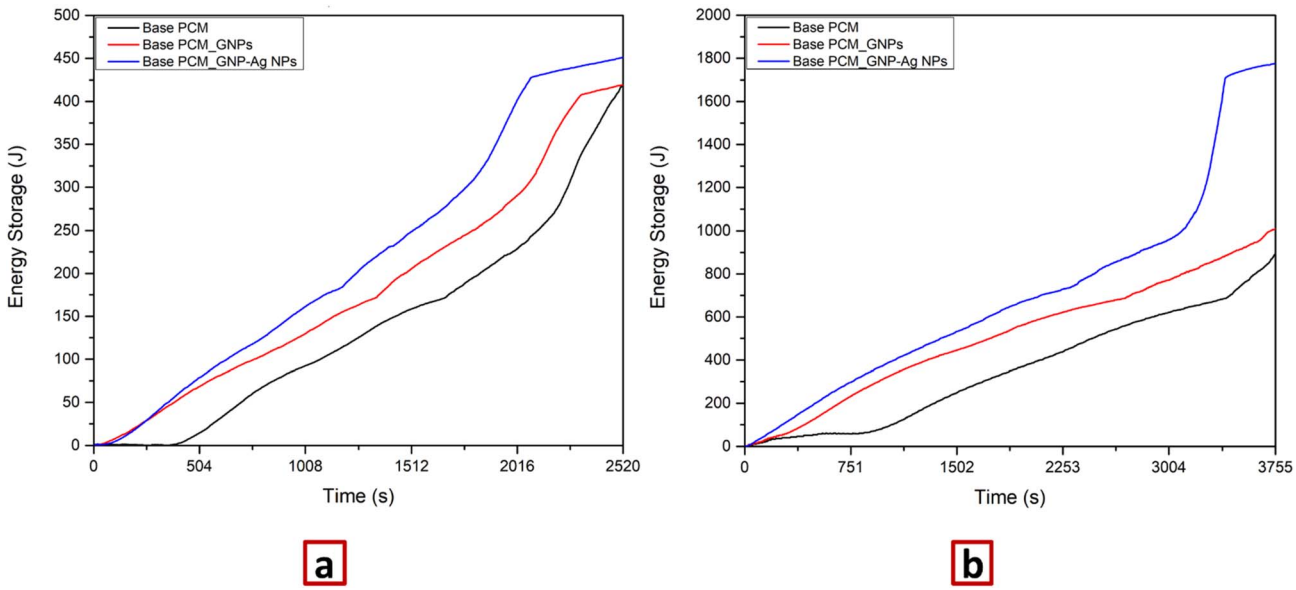

Fig. 6 Total energy storage capacity during melting as a function of time for (a) 3.0 mm cavity test rig (b) 6.0 mm cavity test rig.

1707.825 J at 3400 s at $f_l = 1$, extending to 1775.926 J due to influence of sensible heat. In comparison, the PCM with GNPs and the base PCM exhibited the energy storage capacity value of 1010.993 J and 892.153 J, respectively, with the corresponding 34.31% and 20.52% of the material melted within the same time frame. To verify the thermodynamic consistency of the energy storage results illustrated in Fig. 6, the theoretical potential was calculated using a combined sensible and latent heat formulation as defined in eqn (13). For the 3.0 mm cavity, the theoretical storage limits were established at 481.2 J (base PCM), 478.3 J (PCM with GNPs), and 502.0 J (PCM with GNP-Ag hybrid NPs); the corresponding experimental values of 420.1 J, 419.3 J, and 451.0 J remain strictly within these bounds. Similarly, for the 6.0 mm cavity, the experimental results for the base PCM (892.2 J), PCM with GNPs (1010.1 J), and PCM with GNP-Ag hybrid NPs (1775.3 J) are well-aligned with their respective theoretical limits of 1924.7 J, 1913.2 J, and 2008.0 J. These results confirm that the system adheres to the principle of energy conservation and accurately reflects the non-isothermal nature of the phase change process. The close agreement between the theoretical and experimental values further validates the reliability of the thermal charging measurements and the effectiveness of the NP enhancements. In conclusion, while all three samples can store thermal energy, the NP-impregnated PCMs offer a clear advantage. The PCM impregnated with GNP-Ag hybrid NPs in the 3.0 mm cavity test rig demonstrates superior performance due to its faster absorption rate, higher storage capacity, and ability to handle larger heat transfer distances typically encountered in practical battery module applications.

These findings highlight the potential of NP-embedded PCMs for improved thermal management efficiency in battery systems or energy storage systems. From the above analysis, the evaluation of two cavity-size test rigs prioritized the 3.0 mm cavity test rig for in-depth dimensionless analysis for two primary reasons: (i) it more accurately simulates the actual spatial gaps and high-density packing configurations characteristic of modern lithium-ion battery modules, and (ii) it provided a better-defined thermal boundary layer with consistent and complete phase transitions. The larger 6.0 mm cavity rig exhibited challenges with temperature distribution, heat dissipation, and phase change, potentially due to the larger sample volume. Larger cavity volumes can exhibit greater non-uniformity and multi-cellular convection patterns that complicate the isolation of hybrid NP effects on the overall heat transfer coefficient ($U_{overall}$). Consequently, the 3.0 mm cavity rig's-controlled environment offers a more robust platform for a deeper examination of the underlying heat transfer phenomena and the synergistic role of GNP-Ag hybrid in enhancing thermal management efficiency.

To gain a deeper understanding of the heat transfer processes governing phase change within the chosen 3.0 mm cavity test rig, a comprehensive suite of dimensionless numbers is meticulously analyzed. The implementation of dimensionless parameters such as the Nusselt (Nu), Rayleigh (Ra), Stefan (Ste), and Fourier (Fo) numbers is a well-established methodology for identifying the non-linear coupling between heat conduction and buoyancy-driven convection during phase transition. As demonstrated by Shatikian *et al.*,[52] these parameters are essential for evaluating the internal thermal resistance of encapsulated PCMs and predicting the efficiency of the energy storage process under varying heat flux conditions. In conjunction with these dimensionless metrics, the overall heat transfer coefficient ($U_{overall}$) is evaluated to directly quantify the effectiveness of energy transport between the heater surface and the PCM, serving as a critical dimensional indicator of the material's heat exchange capacity. Each parameter sheds light on a specific aspect of heat transfer, collectively enabling a holistic understanding of the system's performance.

The $U_{overall}$ and Nu quantify the intensity and nature of convection within the cavity and provide insights into fluid motion's role in facilitating heat transfer. Ra is crucial for assessing buoyancy forces and potential flow regime transitions (laminar to turbulent) within the cavity, which are critical for understanding the dominant heat transfer mechanisms. Ste capture the influence of phase change phenomena on heat transfer, allowing them to quantify the relative significance of the latent heat associated with the phase transition. Finally, Fo indicates the relative importance of heat conduction compared to the rate of temperature change. By carefully analyzing these values within the well-defined system of the 3.0 mm cavity, the influence of GNP-Ag hybrid NPs on the composite's thermal behavior is analyzed. This in-depth analysis aspires to establish a robust foundation for optimizing the material's performance and broadening its applicability in diverse thermal management scenarios.

Fig. 7a, demonstrates a significant enhancement in overall heat transfer coefficient ($U_{overall}$) for the composite material impregnated with GNP-Ag hybrid NPs compared to the PCM with GNPs and base PCM. This is evident when considering the temperature–time plot for the heater surface (as shown in Fig. 4a). Because the thermal conductivity of the copper heating surface ($k \approx 400$ W m^{-2} K^{-1}) is significantly higher than that of the base PCM ($k \approx 0.3$ W m^{-2} K^{-1}), the conductive resistance of the wall is mathematically negligible, allowing $U_{overall}$ to accurately quantify the system-level thermal responsiveness.

At 1685 s, the base PCM exhibited a $U_{overall} = 122.961$ W m^{-2} K^{-1}. This was observed when the heater surface temperature was 56.259 °C, resulting in a temperature difference (ΔT) of 5.776 °C between the heater wall and the outer PCM surface. As ΔT increased to 9.594 °C at 2190 s, the overall heat transfer coefficient decreased to 74.024 W m^{-2} K^{-1}, with the heater surface temperature rising to 64.464 °C. This suggests that the base PCM's heat transfer efficiency decreases as the temperature difference increases. The PCM with GNPs demonstrated a higher $U_{overall}$ value of 241.122 W m^{-2} K^{-1} at 1555 s. This occurred when the heater surface temperature was 54.805 °C, corresponding to a ΔT of 2.945 °C. As ΔT increased to 4.97 °C at 2105 s, the overall heat transfer coefficient decreased to 142.902 W m^{-2} K^{-1}, with the heater surface temperature rising to 61.86 °C. The addition of GNPs to the PCM appears to enhance its thermal stability, as evidenced by the more gradual decrease in $U_{overall}$ with increasing ΔT. The GNP-Ag hybrid NP embedded PCM exhibited the highest $U_{overall}$ value of 448.800 W m^{-2} K^{-1} at 1195 s. This was observed when the heater surface temperature was 51.418 °C, corresponding to a ΔT of 1.582 °C. As ΔT increased to 3.095 °C at 1840 s, highlighting the synergistic effects of the GNP-Ag hybrid NPs in augmenting both internal transport mechanisms and overall system-level heat transfer performance. The $U_{overall}$ decreased to 229.475 W m^{-2} K^{-1}, with the heater surface temperature rising to 58.871 °C. The superior performance of the PCM with GNP-Ag hybrid NPs suggests that the combination of GNPs and Ag NPs enhances the PCM's heat transfer efficiency. This substantial improvement translates to a more efficient heat dissipation process, making PCM with GNP-Ag hybrid NPs a compelling candidate for applications demanding rapid thermal management, such as battery module cooling.

The dimensional parameters such as Ra and Nu play a pivotal role in elucidating the effectiveness of overall heat transfer performance within these advanced materials.[53] Ra quantifies the ratio of buoyancy-driven forces to viscous forces in fluid flow, providing insights into the dominance of natural convection and the fluid dynamics within the PCM matrix. On the other hand, the Nu represents the ratio of total heat transfer to pure conductive heat transfer, serving as a measure of the effectiveness of the thermal transport mechanisms within the system. From Fig. 7b, for the base PCM, the observed Nu range of 0.683 to 0.411 reflects a conduction-dominated regime. Mathematically, a Nu < 1 in the early and peak melting stages suggests that natural convection is severely hindered by the high viscous forces of the neat paraffin wax matrix. Although the accompanying high Ra values ranging from 7.70×10^5 to 1.26×10^6 underscore a theoretical potential for buoyancy-driven flow, the low Nu values confirm that the heat transfer process is limited by the material's low thermal conductivity. This highlights the critical conductive bottleneck in neat paraffin and sets the stage for investigating NP-induced enhancements.

Further, the incorporation of 0.1% GNP in PCM represents a strategic intervention aimed at augmenting the overall heat transfer efficiency (Fig. 7b). The expanded Nu range of 1.202 to 0.712, coupled with a lower range of Ra values (3.09×10^5 to 5.13×10^5) compared to the base PCM, signifies a noticeable improvement, pushing the system toward a convection-enhanced state. This enhancement can be attributed to the exceptional thermal conductivity of graphene, which facilitates more efficient heat conduction through the PCM matrix. Additionally, the introduction of GNPs modifies the fluid dynamics, promoting enhanced overall heat transfer rates by accelerating internal transport mechanisms within the molten phase.[54] These findings underscore the potential of NP doping to improve thermal management capabilities within battery modules, thereby enhancing their performance and reliability under demanding operating conditions. The incorporation of 0.1% GNP-Ag hybrid NPs represents a multifunctional approach to enhancing heat transfer. The extended Nu range of 2.071 to 1.059, along with comparable Ra values (1.50×10^5 to 2.89×10^5) to GNP-doped PCM formulations, signifies a definitive shift into a convection-dominated regime. As established by Saha and Dutta,[55] the development of Nu–Ra correlations is a robust methodology for demarcating this transition in encapsulated PCMs. The synergistic effect between GNP and Ag NPs offers unique advantages, including enhanced thermal conductivity and modified fluid behavior that effectively disrupts the stagnant thermal boundary layer.

In summary, the analysis of Ra and Nu values provides a comprehensive understanding of the overall heat transfer performance. In the absence of NPs, the base PCM remains conduction-limited with Nu < 1. Introducing GNP improves these values, but the most notable enhancements are observed with GNP-Ag hybrid NPs, showcasing a Nu significantly greater than unity. This underscores the synergistic effects of GNPs and Ag NPs in promoting natural convection and enhancing overall

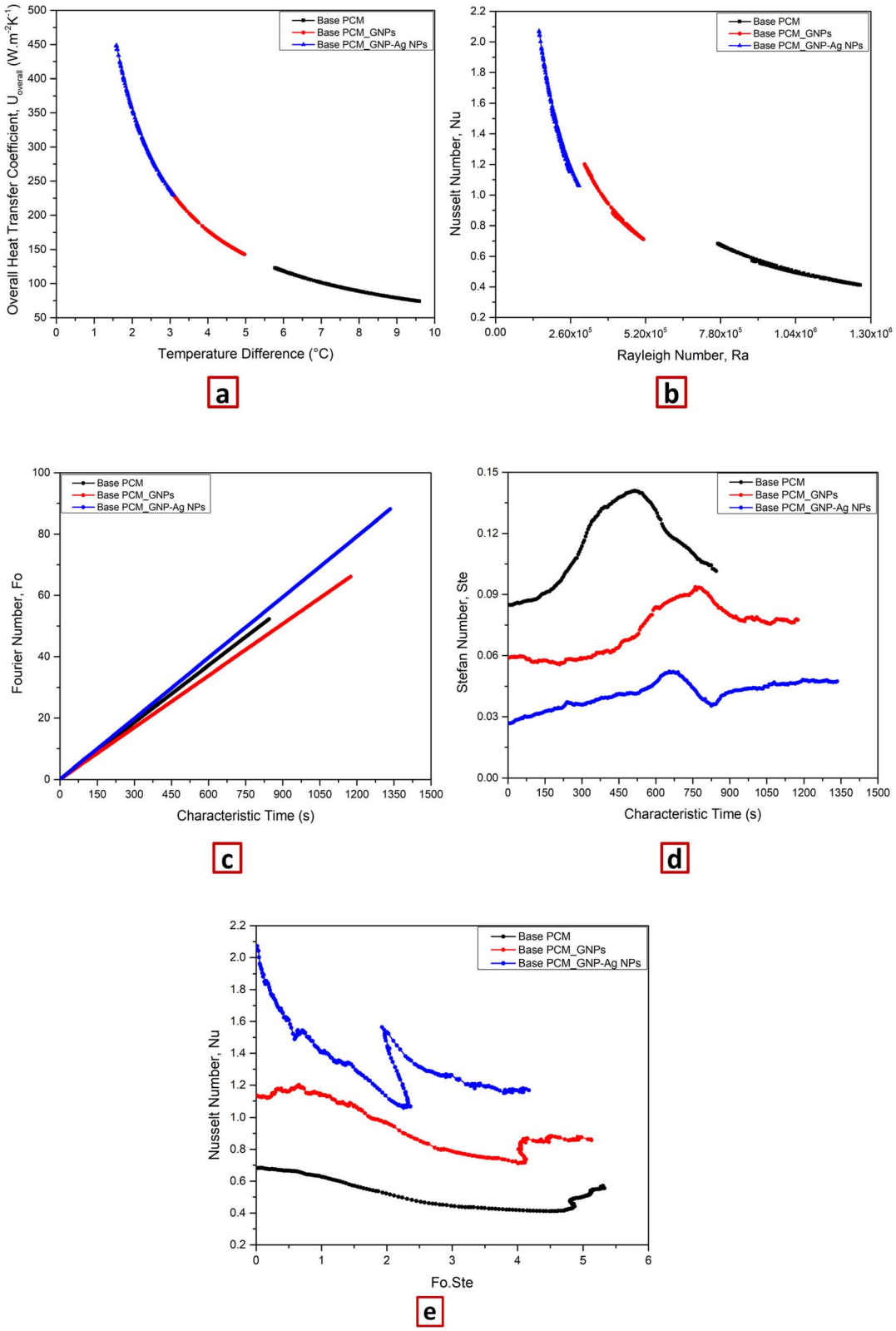

Fig. 7 (a) Overall heat transfer coefficient ($U_{overall}$) over temperature difference (ΔT) (b) Nusselt numbers (Nu) *versus* Rayleigh numbers (Ra) (c) Fourier numbers (Fo) over characteristic time (d) Stefan numbers (Ste) *versus* characteristic time (e) Nusselt numbers (Nu) *versus* product of the Fourier and Stefan numbers (Fo.Ste) for base PCM, GNP impregnated and GNP-Ag hybrid NPs-impregnated PCM samples in 3.0 m cavity test rig.

heat transfer performance. Consequently, for applications requiring augmented thermal management, such as battery modules, the PCM with a low loading of 0.1 wt% GNP-Ag hybrid NPs emerges as the most promising option, offering superior thermal conductivity and heat transfer efficiency of NPs, the base PCM exhibits moderate Ra and Nu values, indicating inherent heat transfer capabilities. Introducing GNP into the PCM matrix enhances both Ra and Nu values, suggesting an improvement in both the buoyancy-driven flow and the overall heat transfer efficiency. However, the most notable enhancements are observed with the incorporation of GNP-Ag hybrid NPs, showcasing significantly higher Ra and Nu value range compared to both the base PCM and GNP-enhanced PCM. This underscores the synergistic effects of GNPs and Ag NPs in promoting fluid motion and enhancing overall heat transfer performance. Consequently, for applications requiring augmented thermal management, such as battery modules, PCM with low loading of 0.1 wt% GNP-Ag hybrid NPs emerge as the most promising option, offering superior thermal conductivity and system-level heat transfer efficiency.

The investigation further delves into the optimization of thermal management in PCMs by analyzing the Fo during the melting process (Fig. 7c). The Fo is a dimensionless number that characterizes the rate of heat conduction. It is defined as the ratio of the heat conduction rate to the rate of thermal energy storage. In this study, PCM with GNP-Ag hybrid NPs exhibited a Fo ranging from 0.33 to 88.11. This range was higher than that of the PCM with only 0.1 wt% GNPs, which had a Fo ranging from 0.28 to 66.12, and the base PCM, which had a Fo ranging from 0.30 to 52.26. The higher Fo for the PCM with GNP-Ag hybrid NPs indicates an enhanced thermal diffusivity, which can be attributed to the synergistic effects of the GNPs and silver NPs. The Ag NPs likely contribute to better heat conduction properties due to silver's high thermal conductivity, while the GNPs may enhance the thermal storage capacity of the PCM.

Insights into the Ste, a crucial parameter reflecting the balance between sensible and latent heat capacities, are provided (Fig. 7d). Sensible heat refers to the heat absorbed or released by a substance during a change in its temperature, while latent heat refers to the heat absorbed or released during a phase change. The balance between these two types of heat capacities is critical for the performance of PCMs, particularly in applications that require efficient heat management, such as battery modules. In this study, the Ste for the base PCM ranges from 0.084 to 0.101. This range indicates that the base PCM has a certain balance between sensible and latent heat capacities. However, when GNPs are embedded into the base PCM, the Ste varies from 0.058 to 0.077. This lower range suggests that the addition of GNPs shifts the balance towards latent heat capacity, potentially enhancing the PCM's ability to absorb and store heat during phase changes. Interestingly, the base PCM integrated with GNP-Ag hybrid NPs exhibits the lowest Ste, ranging from 0.026 to 0.047. This further decrease in the Ste indicates a significant shift towards latent heat capacity. The GNP-Ag hybrid NPs likely enhance the thermal conductivity of the PCM, allowing it to absorb and release heat more efficiently during phase changes. This could lead to a more rapid response to thermal transients, which would be advantageous for maintaining optimal operating temperatures in battery modules. It is crucial to consider the synergistic effects of the incorporated NPs and their impact on the overall thermal performance. For instance, while the lower Ste for the PCM with GNP-Ag hybrid NPs indicates a superior balance between sensible and latent heat capacities, other factors such as thermal conductivity, specific heat capacity, and melting point also play a role in its performance.

The investigation of heat transfer during melting often relies on the independent analysis of the Fourier Fo and Ste numbers. However, for a clearer understanding in the context of thermal management applications, the product of these dimensionless numbers Fo.Ste proves particularly insightful. While Fo characterizes the internal heat diffusion rate, it does not directly address the competition between sensible and latent heat storage. Conversely, Ste highlights this thermodynamic balance but lacks information regarding the characteristic timescale of heat transfer. The product Fo.Ste bridges this gap by serving as a unified dimensionless time scale for correlating phase progression across various test configurations. According to Agrawal,[45] the Fo.Ste product provides a comprehensive characterization of the transient heat conduction and phase-change intensity within cylindrical geometries, serving as a normalized metric for melting progression. A high Fo.Ste value suggests rapid heat diffusion potentially coupled with a preference for sensible heat increase, a scenario less desirable for battery thermal management where the goal is to maintain a stable operating temperature. In contrast, a low Fo.Ste value indicates slower heat transfer within a material that prioritizes latent heat absorption relative to the system's thermal diffusion limit. Following the framework proposed by Stritih,[56] this unified metric effectively quantifies the relative rate of latent heat utilization.

The Nu *versus* the product of Fo.Ste provides additional insights as shown in Fig. 7e. The Nu characterizes the overall heat transfer, while Fo.Ste represents the interplay between internal heat diffusion and the balance of sensible and latent heat storage. The plot data provided further substantiates this interpretation. The PCM with GNP and Ag hybrid NPs, despite having the lowest Fo.Ste value of 4.174, exhibits the highest Nu of 1.167. This high Nu value, coupled with a low Fo.Ste, suggests an efficient overall heat transfer rate and a strong preference for latent heat storage. This combination is ideal for applications like battery thermal management. On the other hand, the PCM with GNP alone shows a medium Nu value of 0.861 for a Fo.Ste value of 5.120, indicating a moderate balance between overall heat transfer and latent heat storage. The base PCM, despite having the highest Fo.Ste value of 5.305, shows the lowest Nu value of 0.571. This suggests a slower rate of overall heat transfer and a preference for sensible heat increase, which might not be as effective for maintaining optimal battery operating temperatures.

To summarize, the comprehensive analysis of temperature distributions, liquid fractions, energy storage capacity, overall heat transfer coefficients ($U_{overall}$), Nu, Ra, Fo, and Ste numbers

reveals that the low-level loading (0.1%) of GNP-Ag hybrid NPs into the base PCM serves as a highly promising candidate for thermal management across diverse energy storage applications. This composite material not only promotes favorable temperature uniformity within the system but also exhibits a superior capability for thermal energy absorption and release due to its higher liquid fraction and energy storage capacity. Furthermore, the enhanced heat transfer efficiency (highest Nu and $U_{overall}$) and faster response to thermal transients (lowest Fo.Ste) make the PCM-GNP-Ag NPs a compelling solution for various energy storage systems beyond just battery modules.

6 Conclusions

In this work, graphene nanoplatelet-silver (GNP-Ag) hybrid nanoparticles (NPs) were successfully synthesized and incorporated at an ultra-low loading of 0.1 wt% into a paraffin-based phase change material (PCM) to enhance its thermal management performance for lithium-ion battery (LIB) applications. Structural characterization (XRD, FESEM, and EDAX) confirmed the successful formation of Ag-decorated GNPs, forming a synergistic thermal transport network within the PCM matrix. The core novel contribution lies in the synergistic 'silver-bridge' architecture, which enhanced effective thermal conductivity by 20.37% and reduces complete melting time by 17.26% compared with bulk PCM, while simultaneously mitigating the viscous suppression of natural convection. Further, the hybrid composite exhibits markedly improved heat dissipation, achieving complete melting at 2085 s in the 3.0 mm cavity and 3400 s in the 6.0 mm cavity, significantly faster than both the base PCM and GNP-only composites. This strategy shifts the system from a conduction-limited bottleneck into a convection-enhanced regime, yielding the highest overall heat transfer coefficient (448.8 W m^{-2} K^{-1}) and Nusselt number (2.07), supported by favourable Fourier and Stefan number correlations. These results confirm the synergistic effect between graphene's high in-plane conductivity and Ag's superior thermal diffusivity, which combinely improved both conductive and overall heat transfer processes, while outperforming traditional geometry-based optimisation in terms of complexity and weight efficiency.

Importantly, this work presents one of the first comprehensive PCM heat transfer assessments conducted under a rigorous ISO/IEC Guide 98-3:2008 (GUM) and ASME PTC 19.1-2013 uncertainty framework. By identifying the mathematical amplification of error in the PCM mushy zone, the analysis validates the accuracy, precision, and reproducibility of all measured parameters and establishes a new metrological benchmark for evaluating the reliability of NP-enhanced thermal storage systems in real-world cylindrical battery modules. The improved energy storage density, rapid phase-change kinetics, and statistically verified performance of the GNP-Ag hybrid NP embedded PCM composite underscore its strong potential for passive cooling applications in lithium-ion battery (LIB) modules. Overall, the study provides key mechanistic and quantitative insights for the rational design of next-generation nanocomposite based PCMs, paving the way for thermally stable, safe, and high-performance energy storage systems.

Author contributions

Balan Akshay: investigation, data curation, software, writing – original draft. Faisal Seyas Seyas Mumthas: investigation, data curation. Manu Mohan: investigation, methodology, supervision, validation, project administration. Vishnu Bhuvanachandran Rajeswari: supervision, resources, validation, project administration. C. Ravikumar: supervision, methodology, validation, writing – review & editing.

Conflicts of interest

The authors declare that they have no known competing financial interests, conflicts of interest or personal relationships that could have influenced the work reported in this paper.

Abbreviations

Ag	Silver
BTMS	Battery thermal management system
DAQ	Data acquisition system
DSC	Differential scanning calorimetry
EDAX	Energy-dispersive X-ray analysis
EDS	Energy dispersive spectroscopy
EV	Electric vehicle
FESEM	Field-emission scanning electron microscope
GNP	Graphene nanoplatelet
GNP-Ag	Graphene-silver hybrid nanoparticle
GUM	Guide to the expression of uncertainty in measurement (ISO/IEC 98-3)
LHTES	Latent heat thermal energy storage
LIB	Lithium-ion battery
NP	Nanoparticle
PCM	Phase change material
TPS	Transient planar source
XRD	X-ray diffractometer
PCM-GNPs	PCM embedded with 0.1 wt% GNPs
PCM-GNP-Ag NPs	PCM embedded with 0.1 wt% GNP-Ag hybrid NPs

List of symbols

$Q_{energy\ storage}$	Total energy storage capacity (J)
r	Radius (m)
Ra	Rayleigh number
Ste	Stefan number
t	Characteristic time (s)
T	Temperature (°C or K)
l	Height of the test rig (m)
y	Measurement result
$U(y)$	Uncertainty of a measurement result
$u_c(y)$	Combined standard uncertainty

k_p^*	Coverage factor corresponding to the desired level of confidence
g	Acceleration due to gravity (m s^{-2})
Fo.Ste	Product of the Fourier and Stefan numbers

Greek symbols

α	Thermal diffusivity (m^2 s^{-1})
β	Thermal expansion coefficient (K^{-1})
μ_d	Dynamic viscosity (mPa s)
ρ	Density (g cm^{-3})
ΔT	Temperature difference (°C or K)

Subscripts

l	Liquid
s	Solid
w,i	Inner wall surface
p,o	Outer PCM surface
o	Onset
p	Peak
i	Initial

Data availability

Supplementary information (SI): the average density, dynamic viscosity, thermal conductivity, specific heat capacity and latent heat of solidification of the base PCM, PCM-GNPs, and PCM-GNP-Ag NPs. No additional datasets were generated or deposited. See DOI: https://doi.org/10.1039/d5ra09895e.

Acknowledgements

We express our sincere gratitude to the Micro/Nanoscale Engineering Research Laboratory (MNERL) at the School of Materials Science and Engineering (SMSE), National Institute of Technology Calicut, India, for their invaluable and extensive support throughout this research. Additionally, we would like to acknowledge the financial assistance provided by the Agency for New and Renewable Energy Research and Technology (ANERT), under reference no. SRI-02/2020-21. This work was also partially carried out using the facilities of UGC-DAE CSR. The authors acknowledge the partial financial support from UGC-DAE CSR through a Collaborative Research Scheme (CRS) project number CRS/2022-23/01/659, and support from Indian Institute of Technology Dharwad, India.

References

1 G. A. Asamoah, M. Korsah, P. G. S. A. Jeyasundar, M. Ahmed, S. Y. Lau and M. K. Danquah, *Sustainability*, 2024, **16**, 9231.
2 Y. Ortiz, P. Arévalo, D. Peña and F. Jurado, *Batteries*, 2024, **10**, 83.
3 G. E. Blomgren, *J. Electrochem. Soc.*, 2016, **164**, A5019–A5025.
4 N. Nitta, F. Wu, J. T. Lee and G. Yushin, *Mater. Today*, 2015, **18**, 252–264.
5 D. Deng, *Energy Sci. Eng.*, 2015, **3**, 385–418.
6 V. Etacheri, R. Marom, R. Elazari, G. Salitra and D. Aurbach, *Energy Environ. Sci.*, 2011, **4**, 3243.
7 A. Calborean, L. Máthé and O. Bruj, *Batteries*, 2025, **11**, 432.
8 S. Lv, X. Wang, W. Lu, J. Zhang and H. Ni, *Energies*, 2021, **15**, 60.
9 S. Ma, M. Jiang, P. Tao, C. Song, J. Wu, J. Wang, T. Deng and W. Shang, *Prog. Nat. Sci.:Mater. Int.*, 2018, **28**, 653–666.
10 K. S. Garud, L. D. Tai, S.-G. Hwang, N.-H. Nguyen and M.-Y. Lee, *Symmetry*, 2023, **15**, 1322.
11 S. Liu, X. Meng, W. Xu and S. Xin, *Mater. Lett.*, 2023, **347**, 134561.
12 Y. Zhang and J. Yi, *Meas. Sci. Technol.*, 1999, **10**, 201–205.
13 A. Sarı, A. Biçer and A. Karaipekli, *Mater. Lett.*, 2009, **63**, 1213–1216.
14 M. Aamer Hayat, Y. Yang, L. Li, M. Bevilacqua and Y. K. Chen, *J. Mol. Liq.*, 2023, **376**, 121464.
15 T. Trisnadewi, E. Kusrini, D. Marta Nurjaya, B. Paul, M. Thierry and N. Putra, *Int. J. Technol.*, 2023, **14**, 596.
16 N. Radhakrishnan and C. B. Sobhan, *Heat Mass Transfer*, 2022, **58**, 1811–1828.
17 H. Yarmand, S. Gharehkhani, G. Ahmadi, S. F. S. Shirazi, S. Baradaran, E. Montazer, M. N. M. Zubir, M. S. Alehashem, S. N. Kazi and M. Dahari, *Energy Convers. Manage.*, 2015, **100**, 419–428.
18 D. Dsilva Winfred Rufuss, L. Suganthi, S. Iniyan and P. A. Davies, *J. Cleaner Prod.*, 2018, **192**, 9–29.
19 Z. Huang, J.-C. Feng and Y. Zhuang, *J. Energy Storage*, 2025, **118**, 116200.
20 Y. Chen, Y. Zhuang, J.-C. Feng and S.-M. Huang, *Appl. Therm. Eng.*, 2023, **232**, 121060.
21 G. Jiang, H. Wen and C. Peng, *Appl. Therm. Eng.*, 2024, **252**, 123686.
22 A. Yadav, A. Pandey, M. Samykano, B. Kalidasan and Z. Said, *Int. Mater. Rev.*, 2024, **69**, 380–446.
23 J. Pereira, A. S. Moita and A. L. N. Moreira, *Molecules*, 2023, **28**, 5763.
24 A. Rahmani, M. Dibaj and M. Akrami, *Batteries*, 2024, **10**, 265.
25 P. Sivasamy, A. Devaraju and S. Harikrishnan, *Mater. Today: Proc.*, 2018, **5**, 14423–14431.
26 L. Syam Sundar, E. Jassim and F. Djavanroodi, *Materials Horizons: from Nature to Nanomaterials*, 2023, pp. 45–69.
27 F. Mebarek-Oudina and I. Chabani, *Energies*, 2023, **16**, 1066.
28 I. Zahid, M. Farooq and M. Farhan, *Mater. Horiz.*, 2023, 11–44.
29 E. Grimonia, M. R. C. Andhika, M. F. N. Aulady, R. V. C. Rubi and N. L. Hamidah, *J. Phys.:Conf. Ser.*, 2021, **2117**, 012005.
30 W. Yu, D. M. France, S. Choi and J. L. Routbort, *OSTI OAI*, U.S. Department of Energy Office of Scientific and Technical Information, DOI: 10.2172/919327.
31 *GUIDE 98-3 Uncertainty of Measurement – Part 3: Guide to the Expression of Uncertainty in Measurement (GUM:1995)*, 2008.
32 *ANSI/ASME PTC 19.1-2013, Test Uncertainty*, American Society of Mechanical Engineers (ASME), 2014.

33 L. Achtelik, Temperature Measurement According to DIN EN 60584: What Needs to Be Considered? - ICS Schneider Messtechnik GmbH, https://www.ics-schneider.de/temperature-measurement-according-to-din-en-60584-what-needs-to-be-considered/?lang=en, accessed 22 October 2025.
34 *TEMPERATURE SENSORS TOLERANCES and COLOUR CODING Thermocouple Tolerances and Application Limits*, 2023.
35 *Agilent Technologies Agilent 34970A/34972A Data Acquisition/Switch Unit Service Guide*, Agilent Technologies, 2010.
36 *34970A Data Acquisition/Switch Unit Family 34970A 34972A*, Agilent Technologies, 2010.
37 B. Taylor and C. Kuyatt, *Guidelines for Evaluating and Expressing the Uncertainty of NIST Measurement Results*, 1994.
38 J. P. Holman, *Heat Transfer*, Mcgraw Hill Higher Education, Boston, 10th edn, 2010.
39 L. P. Santos, J. O. Marino Junior, M. D. de Campos and E. C. Romao, *Applied Mathematical Sciences*, 2013, **7**, 6227–6233.
40 M. Trojan, *Encyclopedia of Thermal Stresses*, 2014, pp. 3483–3498.
41 J. Chen, *Math. Probl. Eng.*, 2022, **2022**, 1–12.
42 R. Saeed, J. P. Schlegel, C. Castano and R. Sawafta, Uncertainty of Thermal Characterization of Phase Change Material by Differential Scanning Calorimetry Analysis, *Int. J. Eng. Res. Sci. Technol.*, 2016.
43 C. Pagkalos, M. Gr. Vrachopoulos, J. Konstantaras and K. Lymperis, *E3S Web Conf.*, 2019, **116**, 00057.
44 S. M. Elsherbiny, M. A. Teamah and A. R. Moussa, *Alexandria Eng. J.*, 2017, **56**, 181–187.
45 A. Agrawal, *J. Enhanced Heat Transfer*, 2016, **23**, 315–348.
46 S. Himran, A. Suwono and G. A. Mansoori, *Energy Sources*, 1994, **16**, 117–128.
47 B. L. Joshi, R. Graf, S. Gindra and T. A. Vilgis, *Curr. Res. Food Sci.*, 2021, **4**, 784–799.
48 D. Guarda, F. Wahli, D. Gwerder, J. Martinez-Garcia, A. Stamatiou, J. Worlitschek, S. Mancin and P. Schuetz, *Nondestr. Test. Eval.*, 2022, 508–518.
49 H. Fatahi, J. P. Claverie and S. Poncet, *Appl. Sci.*, 2022, **12**, 12019.
50 S. Sharma, L. Micheli, W. C. Chang, A. Ali Tahir, K. Rajender Reddy and T. K. Mallick, *Appl. Energy*, 2017, **208**, 719–733.
51 M. Ghalambaz, S. A. M. Mehryan, A. Veismoradi, M. Mahdavi, I. Zahmatkesh, Z. Kazemi, O. Younis, M. Ghalambaz and A. J. Chamkha, *Appl. Therm. Eng.*, 2021, **193**, 116945.
52 V. Shatikian, G. Ziskind and R. Letan, *Int. J. Heat Mass Transfer*, 2008, **51**, 1488–1493.
53 L. El Moutaouakil, M. Boukendil, Z. Zrikem and A. Abdelbaki, *Mater. Today: Proc.*, 2020, **27**, 3051–3057.
54 A. Sathishkumar, P. Sundaram, M. Cheralathan and P. G. Kumar, *J. Energy Storage*, 2024, **78**, 110079.
55 S. K. Saha and P. Dutta, *Appl. Therm. Eng.*, 2010, **30**, 2485–2491.
56 U. Stritih, *Int. J. Heat Mass Transfer*, 2004, **47**, 2841–2847.